AD-A050 117 DYNA EAST CORP WYNNEWOOD PA F/G 19/1

SHAPED CHARGE JET STABILITY AND PENETRATION CALCULATIONS.(U)

SEP 77 J CARLEONE, P CHOU, R D CICCARELLI DAAD05-76-C-0773

UNCLASSIFIED DE-TR-77-1 BRL-CR-351 NL

| OF |

AD A050117

END

DATE FILMED

3-78

DDC

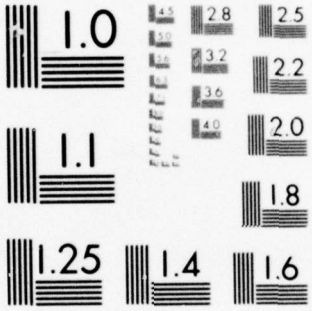

MICROCOPY RESOLUTION TEST CHART
NATIONAL BUREAU OF STANDARDS-1963-A

AD E400 053

AD

12

AD A050117

BRL CR 351

BRL

CONTRACT REPORT NO. 351

SHAPED CHARGE JET STABILITY AND PENETRATION CALCULATIONS

AD No.
DDC FILE COPY

Prepared by

Dyna East Corporation
227 Hemlock Road
Wynnewood, PA 19096

September 1977

DDC
RECEIVED
FEB 17 1978
B

Approved for public release; distribution unlimited.

USA ARMAMENT RESEARCH AND DEVELOPMENT COMMAND
USA BALLISTIC RESEARCH LABORATORY
ABERDEEN PROVING GROUND, MARYLAND

Destroy this report when it is no longer needed.
Do not return it to the originator.

Secondary distribution of this report by originating or sponsoring activity is prohibited.

Additional copies of this report may be obtained from the National Technical Information Service, U.S. Department of Commerce, Springfield, Virginia 22151.

The findings in this report are not to be construed as an official Department of the Army position, unless so designated by other authorized documents.

The use of trade names or manufacturers' names in this report does not constitute indorsement of any commercial product.

(18a) SBIE (19a) AD-E400 053

UNCLASSIFIED

SECURITY CLASSIFICATION OF THIS PAGE (When Data Entered)

REPORT DOCUMENTATION PAGE

READ INSTRUCTIONS BEFORE COMPLETING FORM

1. REPORT NUMBER: BRL CONTRACT REPORT NO. 351

2. GOVT ACCESSION NO.

3. RECIPIENT'S CATALOG NUMBER

4. TITLE (and Subtitle): (6) Shaped Charge Jet Stability and Penetration Calculations

5. TYPE OF REPORT & PERIOD COVERED: (9) Final rept. Jun[redacted]76 – Aug[redacted]977

6. PERFORMING ORG. REPORT NUMBER: (14) DE-TR-77-1

7. AUTHOR(s): (10) Joseph Carleone, Peichi Chou, Robert D. Ciccarelli

8. CONTRACT OR GRANT NUMBER(s): (15) DAAD05-76-C-0773 new

9. PERFORMING ORGANIZATION NAME AND ADDRESS: DYNA East Corporation, 227 Hemlock Road, Wynnewood, PA 19096

10. PROGRAM ELEMENT, PROJECT, TASK AREA & WORK UNIT NUMBERS: (16) 61102A, 1T161102A33E, 04,002A

11. CONTROLLING OFFICE NAME AND ADDRESS: USA Ballistic Research Laboratory, Aberdeen Proving Ground, MD 21005

12. REPORT DATE: (11) SEP[redacted]977 (17) 04

13. NUMBER OF PAGES: 71 (12) 77P.

14. MONITORING AGENCY NAME & ADDRESS (if different from Controlling Office): (18) BRL, SBIE (19) CR-351, AD-E400 053

15. SECURITY CLASS. (of this report): UNCLASSIFIED

15a. DECLASSIFICATION/DOWNGRADING SCHEDULE

16. DISTRIBUTION STATEMENT (of this Report): Approved for public release; distribution unlimited.

DDC RECEIVED FEB 17 1978 B

17. DISTRIBUTION STATEMENT (of the abstract entered in Block 20, if different from Report)

18. SUPPLEMENTARY NOTES

19. KEY WORDS (Continue on reverse side if necessary and identify by block number)

Shaped charges
Fracture
Breakup time
Penetration

20. ABSTRACT (Continue on reverse side if necessary and identify by block number)

This present study focuses on two important aspects of shaped charge mechanics, jet breakup and broken jet penetration. The jet breakup problem is studied from a stability approach. A one-dimensional stability theory for stretching plastic jets is presented. This theory yields a stability criterion which depends on the stress-strain curve of the material. It also gives a critical disturbance wavelength; disturbances of this wavelength grow faster than all others. In addition, the theory shows that the disturbance growth rate increases with decreasing jet

(over)

DD FORM 1 JAN 73 1473 EDITION OF 1 NOV 65 IS OBSOLETE

UNCLASSIFIED

SECURITY CLASSIFICATION OF THIS PAGE (When Data Entered)

i 389 309 JOB

stretching rate and increases with increasing flow stress to density ratio. Comparison with two-dimensional finite difference calculations indicates the general theoretical trends are correct.

The second study examines the problem of broken jet penetration by using two-dimensional calculations to observe the effects of sequential projectile impact on the bottom of a hole in a target. Past experiments show decrease in penetration caused by the increase in gap between projectiles. Calculations of lead projectiles upon lead targets do not show the interference phenomenon which is expected to account for the decrease in penetration. Calculations of copper projectiles at typical shaped charge jet velocities impacting upon steel targets, however, do show the expected interference phenomenon.

Table of Contents

		Page
List of Tables		v
List of Illustrations		vii
Acknowledgment		ix
I.	INTRODUCTION	1
II.	SHAPED CHARGE JET BREAKUP	3
	A. Background	3
	B. One-Dimensional Stability Theory for Stretching Plastic Jets	4
	C. Two-Dimensional Finite-Difference Calculation of Stretching Elastic-Plastic Jets	14
	D. Comparison of One-Dimensional and Two-Dimensional Results	15
	E. Additional Two-Dimensional Stability Results	20
III.	TWO-DIMENSIONAL CALCULATIONS OF MULTIPLE INTERIOR IMPACT PENETRATION	31
	A. Background	31
	B. General Approach	31
	C. Impact of Lead Projectiles on Lead Targets	32
	D. Impact of Copper Projectiles on Steel Targets	41
IV.	CONCLUSIONS	53
V.	REFERENCES	56
	Appendix	59

ACCESSION for
NTIS White Section ✓
DDC Buff Section ☐
UNANNOUNCED ☐
JUSTIFICATION
BY
DISTRIBUTION/AVAILABILITY CODES
Dist. AVAIL. and/or SPECIAL
A

List of Tables

Table		Page
I.	Initial Configuration for segments A,B, and C used in the HEMP calculations	21
II.	Results of HEMP calculations and comparison with experimental breakup time	23
III.	Combinations of Elastic Moduli Used in Calculations	30
IV.	Results of Elastic Moduli Study	30
V.	Summary of the initial conditions of the HELP code calculations	32

PRECEDING PAGE BLANK-NOT FILMED

List of Illustrations

Figure	Title	Page
1	Schematic showing the initial configuration of the jet	8
2	Comparison of relative growth predicted by one-dimensional theory and two-dimensional calculations for two different strain rates, and various length to diameter ratios.	17
3	Comparison of relative growth versus time for one-dimensional theory and two-dimensional calculations with $\eta_0 = .029\ \mu s^{-1}$.	18
4	Comparison of relative growth versus time for one-dimensional theory and two-dimensional calculations with $\eta_0 = .008\ \mu s^{-1}$.	19
5	Schematic position-time plot showing elements A,B, and C used in HEMP calculations.	22
6	HEMP results of a jet with random yield strength distribution throughout.	24
7.	Comparison of HEMP calculations of a stretching jet with two different mesh sizes.	26
8.	A comparison of minimum jet radius histories as predicted by HEMP for two jets with different initial disturbance amplitudes.	27
9.	Relative growth versus time for surface disturbances of four different wavelengths. In all cases, the jets have the same radius and strain rate.	29
10.	Example of the computational grid used in the HELP code calculations of the multiple interior impact problems.	33
11.	Initial configuration of the interior impact of lead projectiles (initial gap = 22mm) onto a lead target.	34
12.	Configuration of lead interior impact (initial gap = 22mm) at 14 μs after initial impact as predicted by HELP code.	35
13.	Configuration of lead interior impact at 30 μs after initial impact (initial gap = 22mm).	36
14.	Configuration of lead interior impact at 47 μs after initial impact (initial gap = 22mm).	37

PRECEDING PAGE BLANK-NOT FILMED

		Page
15	Configuration of lead interior impact at 56 μs after initial impact (initial gap = 22mm).	38
16	Configuration of lead interior impact at 71 μs after initial impact (initial gap = 22mm).	39
17	Penetration depth versus time after initial impact as predicted by HELP for the interior impact of lead projectiles onto a lead target (initial gap = 22mm).	40
18	Initial configuration of the interior impact of lead projectiles (gap = 37mm) onto a lead target.	42
19	Configuration of the lead interior impact (initial gap = 37mm) at 8 μs after initial impact as predicted by HELP code.	43
20	Configuration of the lead interior impact (initial gap = 37mm) at 13 μs after initial impact.	44
21	Configuration of the lead interior impact (initial gap = 37mm) at 24 μs after initial impact.	45
22	Configuration of the lead interior impact (initial gap = 37mm) with a lower target yield strength at 19 μs after initial impact as predicted by HELP code.	46
23	Configuration of lead interior impact (initial gap = 37mm, lower yield strength) at 23 μs after initial impact.	47
24	Configuration of lead interior impact (initial gap = 37mm, lower yield strength) at 29 μs after initial impact.	48
25	Initial configuration of the interior impact of copper projectiles onto a steel target (initial gap = 14mm).	49
26	Configuration of the copper-steel interior impact problem at 4 μs after initial impact as predicted by HELP code (initial gap = 14mm).	50
27	Configuration of the copper-steel interior impact at 9 μs after initial impact (initial gap = 14mm).	51

Acknowledgment

The authors would like to express appreciation to Robert Jameson, Andrew Dietrich and William Walters of BRL for supplying experimental data to guide the present study and also for the many helpful discussions and suggestions during the course of this work. We would also like to thank Michael Khalil of Dyna East for his help with many of the computer calculations contained here.

I. INTRODUCTION

For the past several years, considerable effort has been placed on determining the basic mechanisms in shaped charge jet formation, breakup, and penetration. Various approaches, including experimental, analytical, and numerical, have been used to treat the shaped charge problem. Several aspects of shaped charge mechanics, especially the breakup phenomenon, are still not well understood. The present study will focus on two of these aspects, jet breakup and broken jet penetration.

In [1-3], we have presented the results of initial studies on the jet breakup phenomenon. Formulas for jet strain and jet radius were developed and radiographs of broken jets measured. This work was extended in [4] to include a larger cross-section of experimental data which yielded an empirical correlation (design curve) indicating that jet breakup time increases with increasing jet radius, a general trend expected from linear scaling. Further, because of the resemblance of shaped charge jet breakup and liquid jet breakup, the breakup problem was also approached as an instability problem. In [4], we have shown that the classical stability analyses do not apply to shaped charge jets. We then performed two-dimensional finite-difference calculations using the HEMP code [5] to simulate stretching elastic-perfectly plastic jets. These calculations [4] show that the shaped charge jet is indeed subject to an instability which causes surface disturbance growth and eventual jet breakup. Furthermore, it was found that the driving force for the instability was caused by the material strength of the jet and not the surface tension as in a classical liquid jet. The existence of a critical (i.e. most unstable) wavelength in shaped charge jets was indicated by this numerical study. Related work by Karpp and Simon [6] has also shown the existence of a critical wavelength and the importance of jet strength. These studies, [4] and [6], have shown the range of the critical wavelength to jet diameter ratio <u>at its time of initiation</u> to be $1.5 < (\lambda/d)_{crit} < 2.5$. Of course, by the time the jet breaks, this surface "wave" will be stretched out so that the final aspect ratio of the particles will be larger.

In this report we will present the results of our current study on jet breakup. This study is a continuation of the stability analysis of shaped charge jets. A one-dimensional stability theory for stretching plastic jets is presented which includes the essential effects controlling stability indicated by the two-dimensional numerical computations. Further, two-dimensional calculations of additional factors affecting jet stability are presented.

The second topic of this report, sequential projectile impact and penetration, is an idealized model which simulates broken shaped charge jet penetration. In the past, experiments were conducted at Drexel University [7-10] to study the effect of sequential projectiles impacting the bottom of a pre-drilled hole in a target. These experiments showed in general that the total penetration decreased as the gap between the projectiles increased. "Post mortem" examination of the targets indicated that the probable cause for this was the interference between the trailing projectile and the occlusion or "back flow" caused by the leading projectile.

In this report, a numerical study of sequential interior impact using the HELP code [11] is presented. The goal of this study is to determine the mechanisms involved in the sequential impact process. The experiments of [8-10], which use low speed (1 mm/μs) lead projectiles and lead targets, are simulated by numerical calculations. The numerical computation of copper projectiles, having dimensions of typical shaped charge jet segments, impacting at typical jet velocities onto steel targets is also presented in this study.

In Section II, the results of the breakup study are presented. The sequential projectile impact calculations are given in Section III. Finally, conclusions and recommendations for future study on these topics are presented in Section IV.

II. SHAPED CHARGE JET BREAKUP

In this section, the details of our current study on shaped charge jet breakup will be presented. A new one-dimensional stability theory will be derived and comparison with two-dimensional numerical calculations will be made. Additional factors affecting jet stability using two-dimensional calculations will also be presented.

A. Background

In a typical shaped charge with a conical metallic liner, the ensuing jet travels fastest at the tip with the velocity decreasing in an approximately linear fashion to the rear of the jet [12]. This velocity gradient causes the jet to stretch. Because of this stretching, a series of surface disturbances or "necking" regions eventually develops along the length of the jet. Finally, these necked regions fail and the jet breaks into a series of segments [13-14]. In this report we will study the stability and growth of such disturbances in shaped charge jets.

In the study of flash radiographs of metallic jets, we have observed that there exists a remarkable resemblance between the breakup process in shaped charge jets and that in liquid jets. This resemblance is reported in [4] and [15]. It is a well known fact that for liquid jets this breakup is caused by a surface instability. The subject of liquid jet instability has been investigated by many researchers over the past century [16-21]. These investigations have shown that for a given liquid jet diameter there exists a critical wavelength of the surface disturbance which causes the amplitude of the disturbance to become unstable and grow without bound. The primary driving force for this instability is the surface tension of the liquid.

There are some very significant differences between the classical liquid jet breakup and shaped charge jet breakup, however. In the metallic shaped charge jets surface tension is not an important factor. The major driving force for the disturbance growth is caused by the strength of the jetting metal. In addition, the shaped charge jets are stretching at very high rates of strain. Most of the classical analyses of liquid jets deal with non-stretching jets. The studies which do treat stretching [22,23] neglect the inertia terms in the governing equations. This approximation may be valid for relatively low strain rates, such as those encountered in drawing threads. However for the rates encountered in shaped charge jets, the effect of inertia is of significant importance. Note that a direct extension of the stretching theories of Tomotika [22] or Mikami [23] to include inertia terms and jet strength is a difficult and cumbersome task. This is due to their formulation which is essentially a two-dimensional axisymmetric spatial (Eulerian) formulation that is later reduced to one dimension by assuming a periodic solution along the jet length.

In previous reports [3,4], we have demonstrated that the concepts of surface instability may be applied to elastic-plastic shaped charge jets through the use of the two-dimensional finite difference calculations.

Various factors such as yield strength, density, disturbance wavelength, and random disturbances were considered. The major results of the stability study presented in [4] may be briefly stated as:

1. Jets with higher yield strengths break sooner, all else being equal.
2. Jets with lower densities will break sooner, all else being equal.
3. For the shaped charge jet calculated, there is a critical time for the growth of the disturbance amplitude. Disturbances introduced early do not grow appreciably before this time, but grow rapidly after this critical time. Disturbances introduced after this time also grow rapidly.
4. A critical wavelength (or a range of wavelengths) exists; disturbances having this wavelength grow faster than all others. The length of the broken jet segment caused by this critical wavelength is in the range of measured jet segment lengths.
5. When irregular, or random, surface disturbances are introduced, the growth is again dominated by the disturbance component with the critical wavelength. The jet surface grows into a shape similar to that obtained if only the wave with the critical length were introduced.

Further, in a recent paper [15], we have also presented a one-dimensional stability theory for a plastic stretching jet. This theory predicts all of the pertinent stability effects indicated by the two-dimensional calculations except that of critical wavelength.

In the present study, two approaches will be applied to the problem of shaped charge jet stability. The first is an improved one-dimensional theoretical analysis which will predict a critical wavelength. This is accomplished by incorporating a stress distribution along the axis of the jet which accounts for the "stress concentration" at the "necked" region. The derivation of this improved theory is presented in the next sub-section.

The second approach is the continued use of two-dimensional finite difference calculations to study additional effects such as a random distribution of strength or velocity throughout the jet, elasticity, etc., as well as for comparison with one-dimensional results.

B. One-Dimensional Stability Theory for Stretching Plastic Jets

1. Conservation Equations

For the one-dimensional description of the jet motion, it is more convenient to use the Lagrangian coordinate. The two independent variables involved are the time variable and a variable attached to the original axial position of the mass particles in the jet. Following

Courant and Friedrichs [24], we define a material coordinate a, which assigns a position to each material particle of the jet and remains with that particle as follows

$$a = \frac{1}{\rho_0 A_0} \int_{x(0,t)}^{x(a,t)} \rho A \, dx \tag{1}$$

where ρ is the density of the jet, A is its cross-sectional area, ρ_0 is the initial density, A_0 is the initial cross-sectional area of the undisturbed jet, and x is the spatial coordinate along the axis of the jet fixed to the laboratory in the Eulerian sense. Note that the area A is a function of both location x and time t; this is different from the one-dimensional flow within fixed rigid walls. From this definition we can immediately write the continuity equation, or conservation of mass equation, for an arbitrary element of jet as

$$a_x = \rho A / \rho_0 A_0$$

or

$$\rho A x_a = \rho_0 A_0 \tag{2}$$

where subscripts a and x indicate differentiation. Assuming that the normal component of stress in the axial direction σ is the only non-zero stress during the motion of the jet and that this stress σ is the average of the axial stress over any cross-sectional area, we then perform a momentum balance over an arbitrary element of jet to obtain

$$\rho A \, x_{tt} = \sigma A_x + A \sigma_x \tag{3}$$

or, in terms of the material coordinate a as follows

$$\rho_0 A_0 \, x_{tt} = (\sigma A)_a \tag{4}$$

where the subscript t indicates material time differentiation (i.e. following a material particle). Equations (2) and (4) are the conservation of mass and momentum equations in terms of the independent variables a and t. The specification of a constitutive equation will complete the system of governing equations.

2. Definition of Strain

In the study of one-dimensional stretching problems (e.g. the tension test), two types of strain are typically used (see, e.g. Malvern [20]). The engineering or conventional strain is defined as

$$de = d\ell / \ell_0 \tag{5}$$

where de represents the conventional strain increment, $d\ell$ represents the change in length, and ℓ_0 is a reference, or initial, length. This expression is usually integrated from ℓ_0 to ℓ to obtain $e = (\ell - \ell_0)\ell_0$. Note that in our present development this engineering strain may be equivalently defined as e = (dx-da)/da.

The second strain definition usually encountered is the logarithmic, true or natural strain. This is defined by

$$d\varepsilon = d\ell/\ell \tag{6}$$

where $d\varepsilon$ is the natural strain increment. The obvious difference is that in this definition the deformed, or current, length is used as a basis. Upon integration, we obtain $\varepsilon = \ln(\ell/\ell_0)$, where ℓ_0 is again the original length. Using the conservation of mass, we can express the natural strain as

$$\varepsilon = \ln \frac{\rho_0 A_0}{\rho A} . \tag{7}$$

For an incompressible deformation we have

$$\varepsilon = \ln(A_0/A). \tag{8}$$

Since most empirical stress-strain functions are usually expressed in terms of natural strain, we will employ the definition of Eq. (6) in this paper. However, we may have just as easily used engineering strain to obtain the same final results.

3. Constitutive Equation

For a one-dimensional plastic formulation, it is sufficient to prescribe a uniaxial stress-strain curve as a description of the material properties. Let us consider a universal stress-strain curve given by the function

$$T = T(\bar{\varepsilon}) \tag{9}$$

where T is the effective true stress and $\bar{\varepsilon}$ is the effective true or natural strain (see Malvern [25], pg. 364ff. for definitions of effective stress and strain to be used with the Mises yield condition). In a truly one-dimensional stress problem, e.g. uniaxial tension, the effective stress and strain simply reduce to the axial components of stress and strain respectively. Thus, Eq. (9) may be obtained from a uniaxial tension test. Some older authors (see, e.g., Bridgman [26]) use the term "flow stress" for the true stress when the other stresses vanish. Thus the stress-strain law given by Eq. (9) is the flow stress as a function of axial strain in a one-dimensional sense when no necking occurs. At present we will not specify the actual form of Eq. (9).

The material is also assumed to be incompressible so that

$$\rho = \rho_0 = \text{const.} \tag{10}$$

4. Stretching Jet without Surface Disturbance

Let us first formulate the initial and boundary conditions that most closely describe the stretching jet of the shaped charge without surface disturbances. The solution of this problem will provide a "base solution" upon which we can superimpose a "disturbance solution" to study the stability.

In the jet without surface disturbances, it is valid to assume that the stress field is truly one-dimensional with $\sigma = T(\varepsilon)$. Using this fact together with Eqs. (4),(8),(9), and (10) we have the following final form of the momentum equation

$$\rho_0 A_0 \, x_{tt} = (T - \frac{dT}{d\varepsilon}) A_a . \tag{11}$$

Equations (2) and (11) are the governing equations for the one-dimensional stretching problem without surface disturbances in terms of the dependent variables x and A.

We may assume that one end of the jet is fixed without any loss of generality. The other end of the jet is assumed to move at a constant velocity V_0. Initially, the velocity varies linearly between the ends. The initial cross sectional area of the jet is A_0, a constant; the initial length of the jet is L_0. It is convenient to define an <u>initial stretching rate</u> as $\eta_0 = V_0/L_0$. This configuration is depicted in Fig. 1. Mathematically we express these boundary conditions as

$$x_t = 0 \quad \text{at} \quad a = 0 \tag{12}$$

$$x_t = \eta_0 L_0 \quad \text{at} \quad a = L_0 \tag{13}$$

and the initial conditions as

$$x_t = \eta_0 a \quad \text{at} \quad t = 0 \tag{14}$$

$$A = A_0 \quad \text{at} \quad t = 0. \tag{15}$$

It can be shown that the solution

$$x = a(\eta_0 t + 1) \tag{16}$$

$$A = A_0/(\eta_0 t + 1) \tag{17}$$

satisfies the governing equations, Eqs. (2) and (11), and the auxiliary conditions Eqs. (12)-(15). Equations (16) and (17) represent the solution to the stretching jet problem without surface disturbances. Note that this base solution is independent of the constitutive equation and thus Eqs. (16) and (17) are valid for any incompressible material. Also, all jet particles maintain constant velocity at their initial value, with no acceleration, or,

$$x_t = \eta_0 a \quad \text{for} \quad t \geq 0. \tag{18}$$

and the jet area decreases with time but is uniform at any given time.

5. Stretching Jet with Initial Disturbances

Following the familiar approach in studying the hydrodynamic stability of jets, we will introduce a small disturbance upon the base flow and find the solution to the problem with this disturbed initial condition. If the disturbance dies down as time progresses, the flow is stable; if it grows with time, the flow is unstable. Because of the difficulty involved in treating nonlinear equations, we will consider the

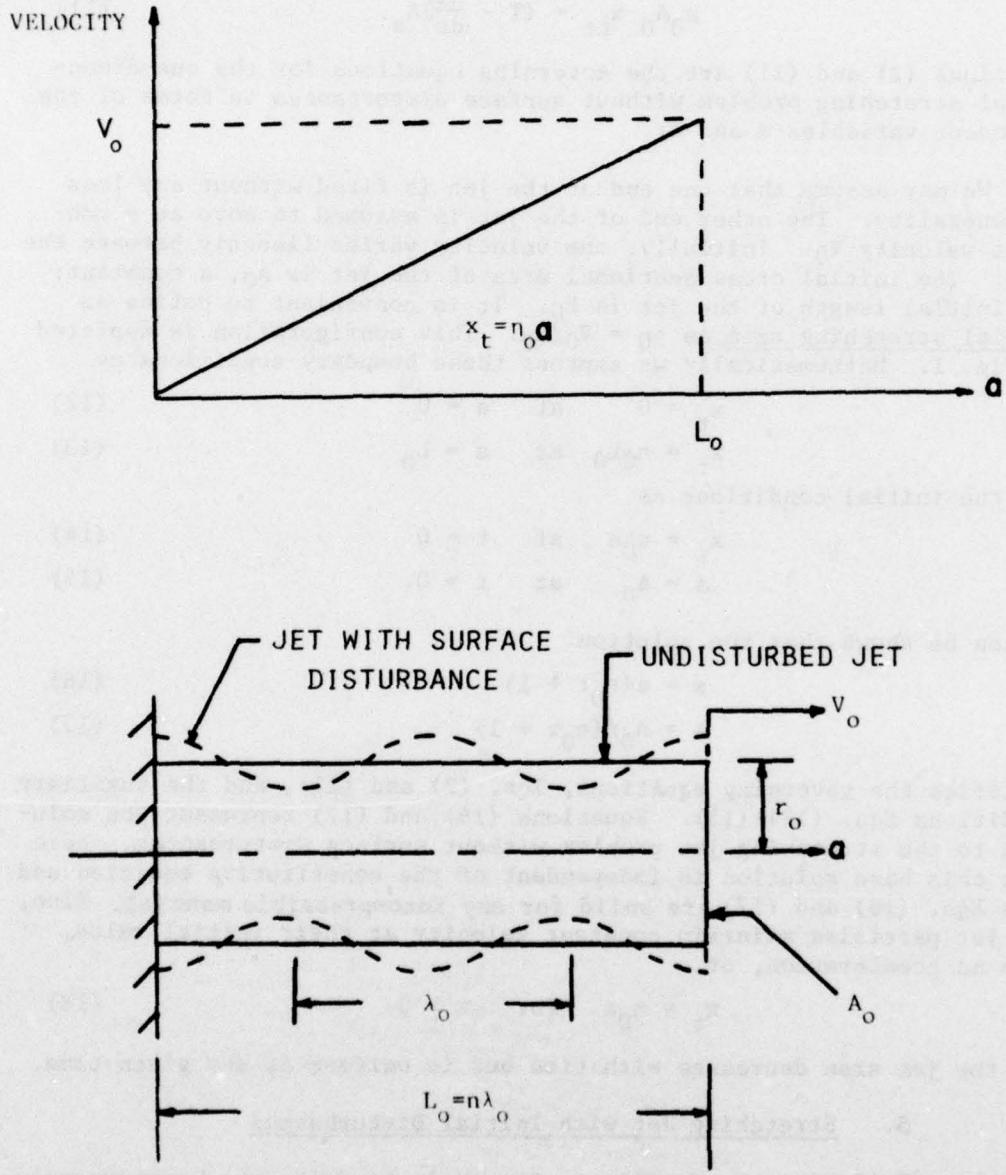

Figure 1. Schematic showing initial configuration of the jet.

linearized problem, which is valid for disturbances of small amplitude, and for small strains after disturbance initiation.

Once a surface disturbance is introduced in the jet, the stress solution is no longer exactly one-dimensional, but, in fact, the average axial stress σ varies along the axis of the jet. For a static tensile test, Bridgman [26] developed the three-dimensional solution in the region of the neck. His result showed that the axial stress at the neck was equal to the flow stress at the free surface and increased to a maximum on the axis. Thus, the average axial stress at the neck is actually higher than the flow stress. Bridgman obtained his results by using the Mises yield criterion and the assumption of isotropic hardening. This is equivalent to postulating a universal stress-strain law such as Eq. (9) (see Malvern [25], pg 364). The result obtained by Bridgman for the average axial stress is given by

$$\sigma = T\left(1 + 2\frac{R}{r_n}\right) \ln \left(1 + \frac{1}{2}\frac{r_n}{R}\right) \tag{19}$$

where r_n is the outside radius at the neck and R is the radius of curvature of the neck.

We now postulate the use of the Bridgman stress solution for our stretching jet problem at any cross-section (i.e. not only at the neck). Further we restrict our result to small disturbances which implies that $1/R \cong \partial^2 r/\partial x^2$. Under these conditions we have for the average axial stress distribution the following

$$\sigma = T\left(1 + \frac{r}{2}\frac{\partial^2 r}{\partial x^2}\right) \tag{20}$$

where $r = r(x,t)$ is the radius of outer disturbed jet surface. Combining Eqs. (4),(8),(9),(10), and (20) we obtain the following form of the momentum equation

$$\rho_0 A_0 x_{tt} = \left(T - \frac{dT}{d\epsilon}\right) A_a + T\left(\frac{A^3 A_{aaa}}{4\pi A_0^2}\right) \tag{21}$$

Note, in writing the final form of this equation we have dropped higher order terms in the derivatives of A (e.g. A_a^2, $A_a A_{aa}$, etc.). This is valid since we eventually will restrict our solution to small surface disturbances and as will be seen these terms will only involve higher order disturbance quantities. Also note that if no surface disturbance exists the second term on the right hand side of Eq. (21) vanishes and Eq. (21) simply reduces to Eq. (11).

The governing differential equations are Eqs. (2) and (21), and the boundary conditions Eqs. (12) and (13) will remain the same. We will first specify the disturbed initial condition for the area A only, and will not impose any specific initial condition for x.

Consider the following disturbed initial condition for the area,

$$A(a,0) = A_0[1 + f_0 \cos ba] \tag{22}$$

where

$$b = \frac{2\pi n}{L_0} = \frac{2\pi}{\lambda_0},$$

n is the number of waves along the given jet length, λ_0 is the initial wavelength of the disturbance, and f_0 is the initial amplitude of the disturbance function which is prescribed to be a small quantity. It will be shown that the following area function can satisfy the governing equations and has the initial value given by Eq. (22)

$$A(a,t) = A_0[1 + f(t)\cos ba]/(\eta_0 t + 1) \tag{23}$$

where f(t) is a function governing the amplitude of the disturbance term and $f(0) = f_0$. Substituting this expression into Eq. (2), we obtain

$$x_a = (\eta_0 t + 1)/[1 + f(t)\cos ba]. \tag{24}$$

If we neglect terms of the order f^2 and higher, then Eq. (24) may be written as

$$x_a = (\eta_0 t + 1)[1 - f(t)\cos ba]. \tag{25}$$

Integrating this expression and using the boundary condition, we obtain for the position

$$x = (\eta_0 t + 1)[a - (f/b)\sin ba]. \tag{26}$$

Substituting the expressions for x and A, Eqs. (26) and (23), and their derivatives into Eq. (21) and neglecting terms of the order f^2 and higher, we obtain

$$(\eta_0 t+1)^2 f_{tt} + 2\eta_0(\eta_0 t+1)f_t - \left[\left(T - \frac{dT}{d\varepsilon}\frac{b^2}{\rho_0}\right) - T\frac{A_0 b^4}{4\pi\,\rho_0(\eta_0 t+1)^3}\right]f = 0. \tag{27}$$

If the function f satisfies Eq. (27), then the corresponding Eqs. (23) and (26) are the solution of the linearized problem of Eqs. (2) and (21), boundary conditions Eqs. (12) and (13), and the disturbance initial condition Eq. (22). The other initial condition on x_t turns out to be

$$x_t = \eta_0 a - \frac{1}{b}[\eta_0 f(0) + f_t(0)]\sin ba \quad \text{at} \quad t = 0. \tag{28}$$

Up to this point we have not considered the form of the stress-strain law Eq. (9). We will now consider two cases, simple work hardening and perfectly plastic.

Case I - Work Hardening

With no loss of generality, we will consider the strain hardening law to be a series expansion about the initial point, $\varepsilon = 0$, $T = \sigma_0$,

$$T(\varepsilon) = \sigma_0 + C\varepsilon + F\varepsilon^2 + \cdots \tag{29}$$

Since we seek a linearized solution, we may restrict our result to small strains from the disturbance initiation. Under this small strain assumption,

$$\begin{aligned} T &\approx \sigma_0 \\ \frac{dT}{d\varepsilon} &\approx C \, . \end{aligned} \tag{30}$$

We further neglect $\eta_0 t$ with respect to 1 in the coefficient of f in Eq. (27) which is consistent with the small strain assumption*. These approximations applied to Eq. (27) yield the following differential equation governing the disturbance function

$$(\eta_0 t+1)^2 f_{tt} + 2\eta_0(\eta_0 t+1) f_t - \frac{b^2}{\rho_0}\left[\sigma_0\left(1 - \frac{r_0^2\, b^2}{4}\right) - C\right] f = 0 \tag{31}$$

Equation (31) is an ordinary differential equation of the Euler type and can be solved by elementary methods. The solution is of the form

$$f(t) = Q(\eta_0 t + 1)^s \tag{32}$$

where Q is an arbitrary constant, and

$$s = \frac{1}{2}\left(-1 \pm \sqrt{1 + 4K}\right) \tag{33}$$

$$K = \frac{4}{\rho_0}\left(\frac{\pi}{\eta_0 \lambda_0}\right)^2 \left\{\sigma_0\left[1 - \left(\frac{\pi\, r_0}{\lambda_0}\right)^2\right] - C\right\} . \tag{34}$$

The disturbance function f(t) will decay with time if s is negative and grow if s is positive. From Eqs. (33) and (34) it can be seen that a positive root of s exists if

$$\sigma_0\left[1 - \left(\frac{\pi\, r_0}{\lambda_0}\right)^2\right] > C \tag{35}$$

---

* Note that we do not neglect $\eta_0 t$ in the other two terms since it is not necessary to obtain a simple solution and no problem is encountered by carrying it.

In our analysis so far, we have assumed that there is an initial state where the strain is zero and the length of the jet is L_0. The stress-strain relation is expanded into a series about this state. This initial state, or initial time, is completely arbitrary. We may consider <u>any time</u> during the jet stretching process as the initial time and the stability analysis presented above is always true. In this sense, σ_0 in Eq. (29) is the flow stress at the time under consideration and C is the slope (or tangent modulus) of the stress-strain curve at that stress level. The stability results, Eqs. (32), (33), and (34) depend only on the values of the stress and the slope of stress-strain curve, and are independent of the value of the strain. Note also that in our derivation the stress is the true stress, or force per unit current area, and the strain is the natural or true strain. In contrast to the more elementary theory [15] which did not account for the stress concentration, the stability results do depend on the initial dimensions r_0 and λ_0. We thus see that there is an initial wavelength which yields a maximum disturbance growth. We define this to be the critical wavelength. By differentiating Eq. (33) with respect to λ_0, holding all other parameters fixed, and setting the result to zero we find the critical wavelength to be given by

$$\left(\frac{\lambda_0}{2r_0}\right)_{crit} = \frac{\pi}{\sqrt{2}}\sqrt{\frac{\sigma_0}{\sigma_0 - C}}, \quad \sigma_0 \neq C \tag{36}$$

We further note that for a critical disturbance given by Eq. (36), the condition for a positive exponent Eq. (35) reduces simply to $\sigma_0 > C$, i.e. if the stress is greater than the tangent modulus.

We may now state the jet stability criterion as follows:

The stability of a stretching jet may vary from time to time. For a jet having a critical disturbance defined by Eq. (36), when the true stress is less than or equal to the slope of the true stress-true-strain curve, the jet is stable; otherwise the jet is unstable. That is, a jet having a critical disturbance is stable if

$$\sigma_0 \leq C. \tag{37}$$

The stability of a jet having a disturbance other than critical is governed by the criterion of Eq. (35). For an unstable jet, any small disturbance will grow, and the rate of growth is governed by the value of K.

It is interesting to note that in the conventional static simple tension tests, the plastic instability criterion [27] is the same as our present one for critical disturbances although completely different physical reasoning was used. In the static case, the critical instability point is defined as the point where the engineering stress vs. engineering strain curve has a zero slope. This point, when transformed on the true stress vs. true strain curve, is the point where $\sigma_0 = C$.

The argument for establishing this static criterion is that when the engineering stress is a maximum, the load carrying capacity of the specimen reaches a maximum. The specimen will stretch to complete failure while the total load is decreasing.

The present disturbance solution yields some very interesting trends. From Eqs. (33) and (34) it can be seen that the larger the value of K, the faster the growth rate. This factor is strongly dependent upon the ratio σ_0/ρ_0. Thus, we see that, in general, for unstable jets the larger the flow stress, the faster the growth rate; the larger the density, the smaller the growth rate. It is interesting to note that the growth rate is inversely proportional to the initial stretching rate η_0; as the stretching rate becomes larger the growth becomes slower.

Case II - Perfectly Plastic

For a perfectly plastic material, Eq. (9) becomes independent of strain and is given by

$$T(\varepsilon) = Y \tag{38}$$

where Y is the yield stress in simple tension and taken as a constant for a given material. Using Eq. (38) together with Eq. (27) and again dropping $\eta_0 t$ with respect to 1 in the f term coefficient, we obtain a differential equation similar to Eq. (31). The solution is again given by Eqs. (32) and (33) but now the definition of K, Eq. (34), is given by

$$K = \frac{Y}{\rho_0}\left(\frac{\pi}{\eta_0\lambda_0}\right)^2\left[1 - \left(\frac{\pi\, r_0}{\lambda_0}\right)^2\right] \tag{39}$$

We again note the existence of a stability criterion based on whether the exponent s is positive or negative. However for perfectly plastic jets, the stability is not based on material properties but only on the initial geometry of the disturbance. From Eq. (39) we see that the jet is stable if

$$\frac{\lambda_0}{2r_0} < \pi/2 \tag{40}$$

otherwise the jet is unstable.

Also, from Eqs. (32), (33) and (39) we note the existence of a critical wavelength. Following the procedure used in the work hardening case we find the critical wavelength for perfectly plastic jets to be given by

$$\left(\frac{\lambda_0}{2r_0}\right)_{crit} = \frac{\pi}{\sqrt{2}} \tag{41}$$

Thus, in the perfectly plastic case the initial critical wavelength is always 2.22 times the initial jet diameter.

Again the same growth trends appear in the perfectly plastic case as was observed in the work hardening case.

6. Complete Stability Solution

In Section IID, we will compare this linearized theory for the case of a perfectly plastic material with a two-dimensional calculation for a particular problem with specific initial conditions. For this purpose, a complete solution to Eq. (31) is needed. The general solution of Eq. (31) is

$$f(t) = Q_1(\eta_0 t + 1)^{s_1} + Q_2(\eta_0 t + 1)^{s_2} \tag{42}$$

where Q_1 and Q_2 are constants to be determined from initial conditions on f, and s_1 and s_2 are the two roots defined by Eq. (33). For this specific problem we impose initial conditions in which the position of the surface is disturbed and at rest. These can be approximated as

$$\begin{aligned} f(0) &= f_0 \\ f_t(0) &= 0. \end{aligned} \tag{43}$$

Using these two conditions, we obtain the following result

$$f(t) = \frac{f_0}{s_2 - s_1}\left[s_2(\eta_0 t + 1)^{s_1} - s_1(\eta_0 t + 1)^{s_2}\right] \tag{44}$$

This disturbance function can now be used to compute the position, velocity, and cross-sectional area for the stretching jet problem with a surface disturbance.

C. Two-Dimensional Finite-Difference Calculation of Stretching Elastic-Plastic Jets

The numerical study of jet stability was undertaken through the use of the two-dimensional code HEMP [5]. The HEMP code is a general purpose code which solves the conservation equations of two-dimensional elastic-plastic flow in plane coordinates or in axisymmetric coordinates. The solution is by the method of finite differences and uses the Lagrangian formulation. The code has the capability of handling many various boundary and initial conditions. In this section we will briefly describe the general approach of applying HEMP to the jet stability problem.

Karpp [6] first applied HEMP code calculations to the problem of a stretching elastic-plastic jet with the surface slightly disturbed. After calculating surface disturbances of various wavelengths, he found a range of most unstable wavelengths with reasonable growth rates. We have applied the same basic method to study the breakup problem in more detail. We have used the HEMP code to study many various aspects of stretching elastic-plastic jets including the effects of yield strength, disturbance initiation time, disturbance wavelength, random surface disturbances, and inertia forces.

For these two-dimensional calculations, a stretching shaped charge jet is modelled by an axisymmetric bar fixed at one end, with the other end moving at a constant velocity. A linear velocity distribution in the axial direction is again imposed as the initial condition, and the surface of the bar is initially perturbed in the shape of a cosine function, as previously shown in Fig. 2. Note that to a first order approximation perturbing the radius is equivalent to perturbing the cross-sectional area as done in the one-dimensional theory Eq. (22). The perturbed surface is free from any tractions and the end surfaces are free of any shear stresses. Let the axial velocity be $v(x,r,t)$, the radial velocity be $u(x,r,t)$, the stress vector on the lateral surface be $\sigma(x,r_s,t)$, and the shear stresses on the end surfaces be $\tau_{rx}(0,r,t)$, $\tau_{x\theta}(0,r,t)$, $\tau_{rx}(L_0,r,t)$, $\tau_{x\theta}(L_0,r,t)$, then the boundary conditions are

$$\begin{aligned} v(0,r,t) &= 0 \\ v(L,r,t) &= V_0 \\ \underset{\sim}{\sigma}(x,r_s,t) &= \underset{\sim}{0} \\ \tau_{rx}(0,r,t) = \tau_{x\theta}(0,r,t) &= \tau_{rx}(L_0,r,t) = \tau_{x\theta}(L_0,r,t) = 0 \end{aligned} \tag{45}$$

and the initial conditions are

$$v(x,r,0) = (V_0/L_0)x \quad \text{and} \quad u(x,r,0) = 0 \tag{46}$$

where r_s is the disturbed surface $r_0 + D_0(\cos 2\pi nx/L_0)$. The calculation of one cycle of the surface wave along the axial direction is sufficient because of the symmetry of the problem.

Using this basic approach we have calculated various problems of stretching jets. Unless otherwise noted, we have considered elastic-perfectly plastic copper jets with an equation of state for copper as specified in the HEMP code. The value of density used was 8.9 Mg/m^3; the elastic shear modulus was taken as 45.6 GPa and the yield stress used was 0.2 GPa.

D. Comparison of One-D and Two-D Results

To compare the results of the linearized one-dimensional theory and the two-dimensional numerical solutions, we have computed several problems having dimensions and stretching rates which span the range of those normally encountered in typical shaped charge jets. More specifically, we have considered two stretching rates in these problems $\eta_0 = 0.029\ \mu s^{-1}$ and $\eta_0 = 0.008\ \mu s^{-1}$. In all cases the initial undisturbed radius was $r_0 = 1.5$mm. All jets were considered to be perfectly plastic with material constants specified in Section IIC. The wavelength λ_0 was varied such that $1.5 < \lambda_0/2r_0 < 6$. In our comparisons we will use the relative growth Δ defined as

$$\Delta(t) = [D(t) - D_0]/D_0 \tag{47}$$

where D(t) is the amplitude of the surface disturbance at time t and D_0 is the initial amplitude. In terms of the disturbance function f, it can be shown that for small disturbances (i.e. small f)

$$\Delta(t) = \frac{f(t)}{f_0\sqrt{\eta_0 t + 1}} - 1. \tag{48}$$

Substituting the one-dimensional solution Eq. (44) into Eq. (48), we see that f_0 is eliminated and thus Δ for small disturbances is independent of the initial disturbance f_0. Figure 2 shows a plot of Δ vs $\lambda_0/2r_0$ at a time of 28 μs after disturbance initiation for both strain rates considered. In this case the two-dimensional solution had $D_0 = 0.001\ r_0$. The two-dimensional solutions show that the critical length to diameter ratio (i.e. the one which yields maximum Δ) varies with the initial strain rate from 1.5 at $\eta_0 = 0.029\ \mu s^{-1}$ to 2.2 at $\eta_0 = 0.008\ \mu s^{-1}$. As discussed above, for perfectly plastic jets, the one-dimensional theory always predicts $(\lambda_0/2r_0)_{crit} = 2.2$ regardless of strain rate. We should also note that Karpp and Simon [6] found $(\lambda_0/2r_0)_{crit} = 2.2$ using HEMP code for jets with strain rates in the range of $0.005\ \mu s^{-1} < \eta_0 < 0.008\ \mu s^{-1}$. Further, the growth predicted by the one-dimensional theory appears in good agreement with the two-dimensional solution at the lower strain rate. At the higher strain rate, $0.029\ \mu s^{-1}$, however, the theory predicts values which are quite low. To exemplify this further Figs. 3 and 4 show plots of Δ vs t for $\eta_0 = 0.029\ \mu s^{-1}$ and $\eta_0 = 0.008\ \mu s^{-1}$ respectively. Both have an initial length to diameter ratio of 2.2. Also in Fig. 3 we show a two-dimensional solution with the initial amplitude increased by a factor of 50 to $D_0 = .05\ r_0$. We see that for this set of conditions the relative growth is also independent of initial amplitude. It is also important to note that, for a given time after disturbance initiation, the linearized solution for the case with higher initial strain rate involves more error than for the case with lower initial strain rate. It is anticipated that a solution which uses the linearized solution for successive time steps will alleviate this problem.

It is interesting to note that, for the small amplitude problem, $D_0 = 0.001\ r_0$, the HEMP code solution indicates that the material is completely in the plastic range. After some initial fluctuation in the solution, HEMP predicts an axial stress at the prescribed yield point 0.2 GPa with the other stresses being negligible. Therefore, neglecting elastic unloading in the theory is a reasonable assumption. For problems with larger disturbance amplitudes, or if we continue the present calculation until the disturbance grows significantly larger, the HEMP solution does not remain completely plastic and an elastic region forms near the ends, where the cross-sectional area is larger. All of the stretching then takes place in the "necked" region. We will discuss the effects of disturbance amplitude and elasticity in more detail in the next section.

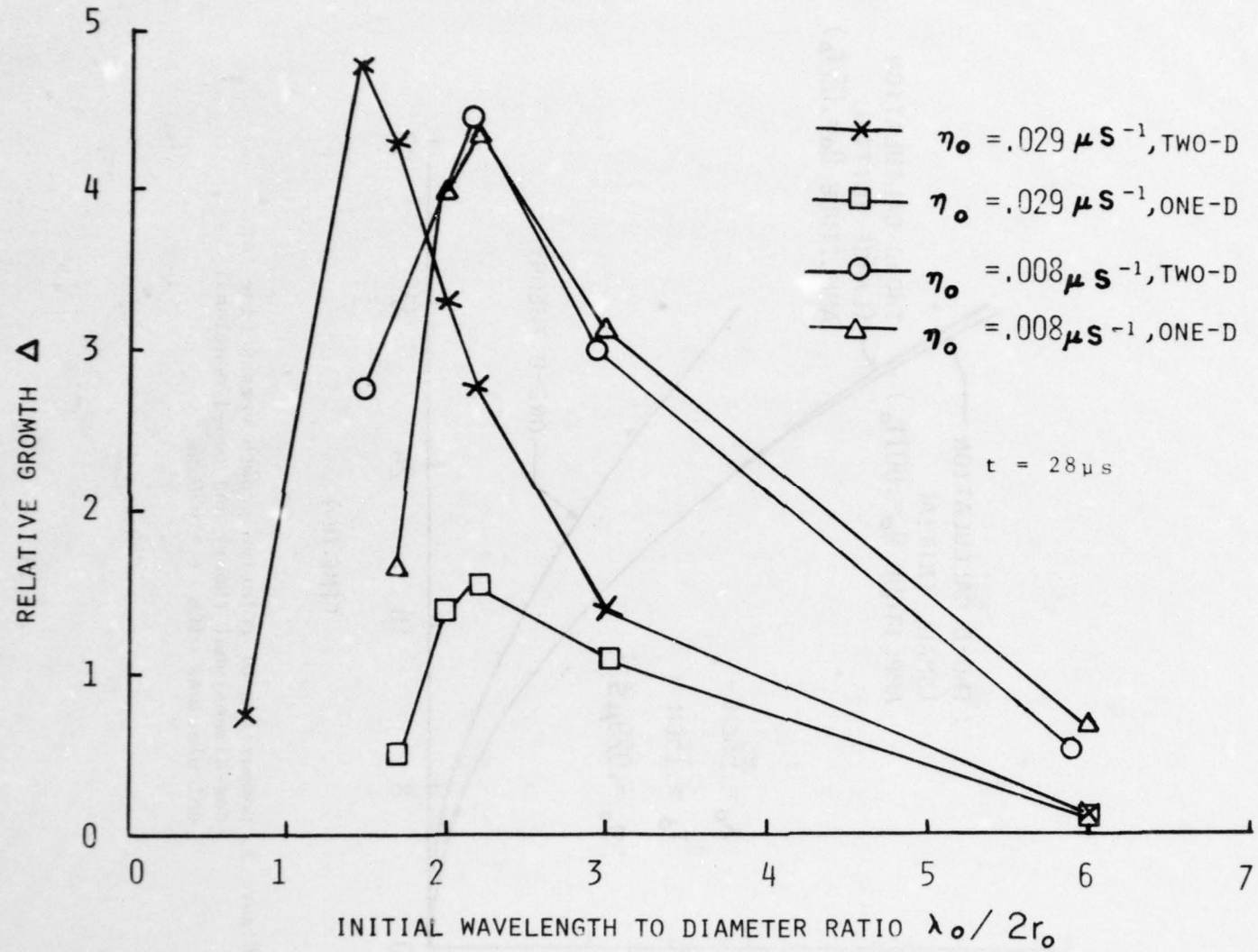

Figure 2. Comparison of relative growth predicted by one-dimensional theory and two-dimensional calculations for two different strain rates and various length to diameter ratios at 28 μs after disturbance initiation.

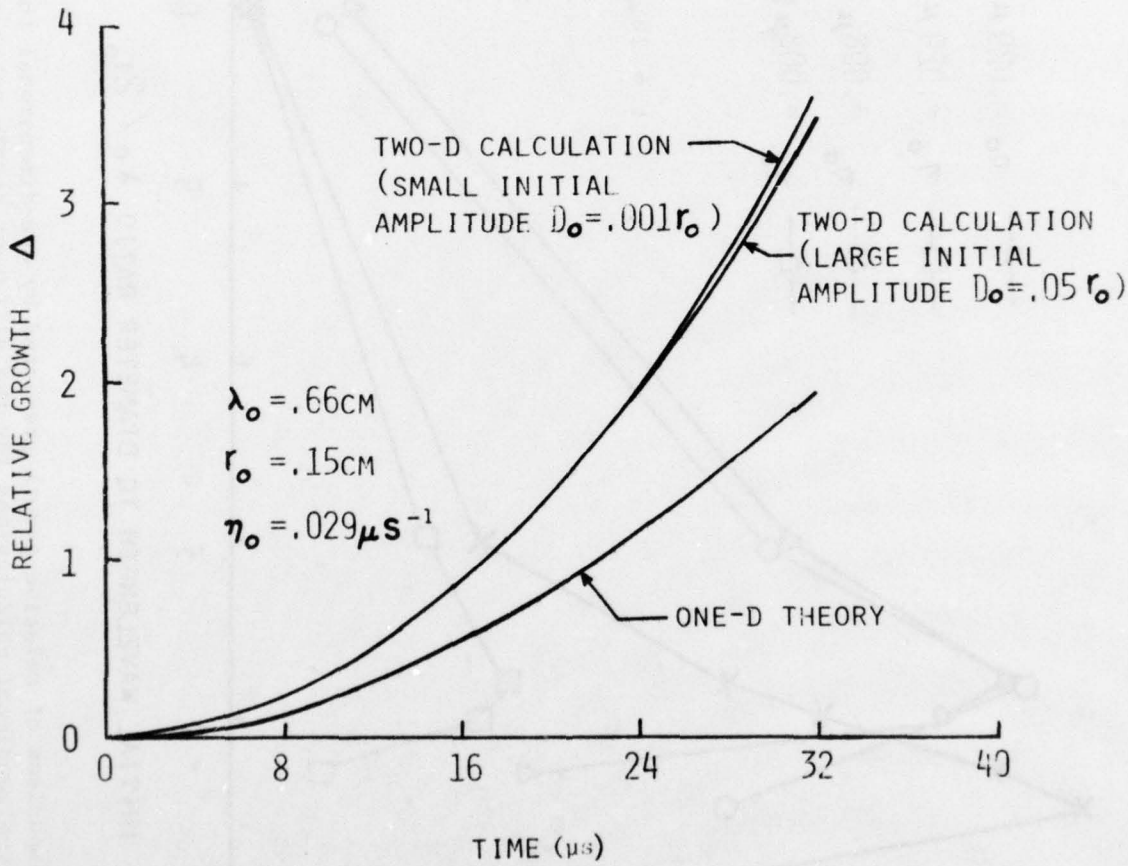

Figure 3. Comparison of relative growth versus time for one-dimensional thoery and two-dimensional calculations with η_o=.029 μs^{-1}.

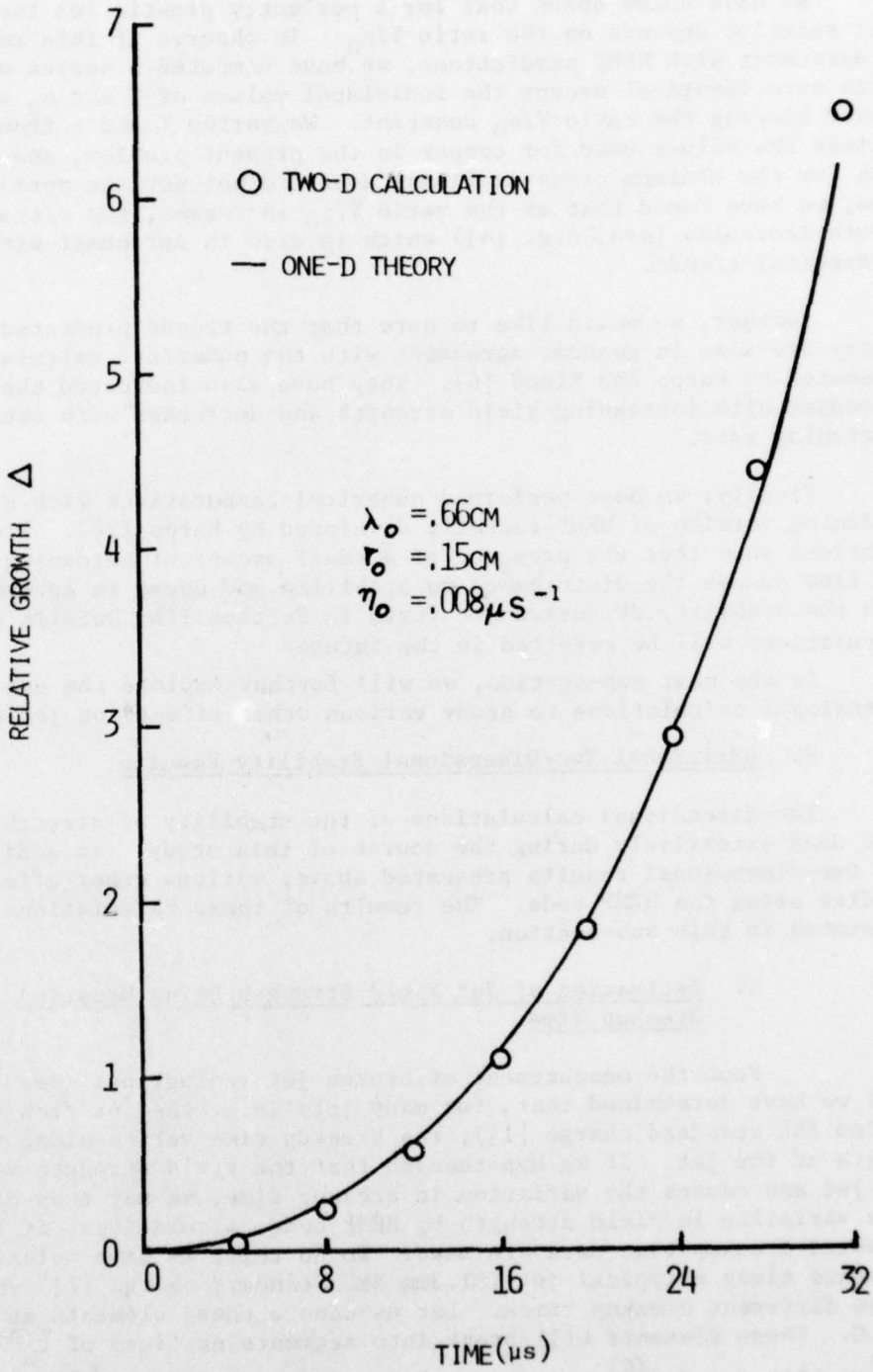

Figure 4. Comparison of relative growth versus time for one-dimensional theory and two-dimensional calculations with η_o = .008μs^{-1}.

We have noted above that for a perfectly plastic jet the theoretical solution depends on the ratio Y/ρ_0. To observe if this result is in agreement with HEMP predictions, we have computed a series of problems which were identical except the individual values of Y and ρ_0 were varied keeping the ratio Y/ρ_0 constant. We varied Y and ρ from 1/3 to 2 times the values used for copper in the present problem, and the solution for the minimum cross-sectional area did not deviate more than 1%. Also, we have found that as the ratio Y/ρ_0 increases, the disturbance growth increases (see, e.g. [4]) which is also in agreement with the theoretical trends.

Further, we would like to note that the trends predicted by the theory are also in general agreement with the numerical calculations presented by Karpp and Simon [6]. They have also indicated that growth increases with increasing yield strength and decreases with increasing stretching rate.

Finally, we have performed numerical computations with a work hardening version of HEMP recently developed by Karpp [28]. These calculations show that the presence of a small amount of hardening during the flow causes the disturbance to stabilize and decay in agreement with the stability criterion set forth in Section IIB. Details of these calculations will be reported in the future.

In the next sub-section, we will further explore the use of two-dimensional calculations to study various other effects on jet stability.

E. Additional Two-Dimensional Stability Results

Two-dimensional calculations of the stability of stretching jets were used extensively during the course of this study. In addition to the two-dimensional results presented above, various other effects were studied using the HEMP code. The results of these calculations will be presented in this sub-section.

1. Estimation of Jet Yield Strength Using Measured Breakup Time

From the measurement of broken jet radiographs (see [1] and [4]) we have determined that, for many jets (e.g. the jet from the 81.3mm BRL standard charge [1]), the breakup time varies along the length of the jet. If we hypothesize that the yield strength varies along the jet and causes the variation in breakup time, we may then determine this variation in yield strength by HEMP code calculations, if the measured breakup time data are used. To do this, we have selected three elements along a typical jet (81.3mm BRL Standard charge [1]) which have three different breakup times. Let us denote these elements as A, B, and C. These elements will break into segments at times of $t_b^{(A)} = 94$ μs, $t_b^{(B)} = 121$ μs and $t_b^{(C)} = 161.6$ μs as determined from the least squares breakup distribution of [1]. These times are based on t = 0 when the detonation wave reaches the cone apex. These elements have average jet

velocities of $V_j^{(A)} = 7.1$ km/s, $V_j^{(B)} = 6.2$ km/s, and $V_j^{(C)} = 4.9$ km/s. Using a one-dimensional model we may trace back these elements to their original position on the cone and also compute their impinging velocity onto the stagnation point during formation. From these one-dimensional calculations we find $\bar{x}^{(A)} = 0.44$, $\bar{x}^{(B)} = 0.51$, and $\bar{x}^{(C)} = 0.60$ and $M^{(A)} = 0.85$, $M^{(B)} = .75$, and $M^{(C)} = 0.62$, where $\bar{x}$ is the axial position from the cone apex divided by the cone height (h) and M is the Mach Number of the impinging flow.

Now, we consider each of these elements to be stretching before breakup and perform HEMP calculations of each. We introduce a sinusoidal surface disturbance as described in Section IIC in each element at a considerable time before the breakup time and observe if the disturbance growth will cause the element to break at the desired breakup time. A schematic position-time plot of this process is shown in Fig. 5. The yeild strength in each element is adjusted until the desired result is obtained. The HEMP code does not have the capability to actually predict a break in the stretching element. We prescribe a somewhat arbitrary criterion for a "necked" section to break which is when the necked cross-sectional area is 10% of the average maximum cross-sectional area of the jet segments as measured from jet radiograph. The initial configuration for each element of jet used in the HEMP calculations is given in Table I as is the time of disturbance initiation t_i. The difference in velocity between the two ends of each element ΔV_j is also given and was computed using the velocity gradient in the jet at the time t_i. The results of the HEMP computations are shown in Table II, where we see that strengths of $Y_0^{(A)} = 0.12$ GPa and $Y_0^{(B)} = 0.066$ GPa and $Y_0^{(C)} = 0.036$ GPa cause breakup times very close to the experimental values.

Table I
Initial configuration for segments A,B, and C used in the HEMP calculations.

element / property	A	B	C
initial length (mm)	4.79	4.65	4.59
initial radius (mm)	1.60	1.55	1.53
ΔV_j (mm/μs)	.147	.105	.078
t_i (μs)	43.6	54.8	74.3
initial disturbance amplitude (mm)	.080	.078	.077

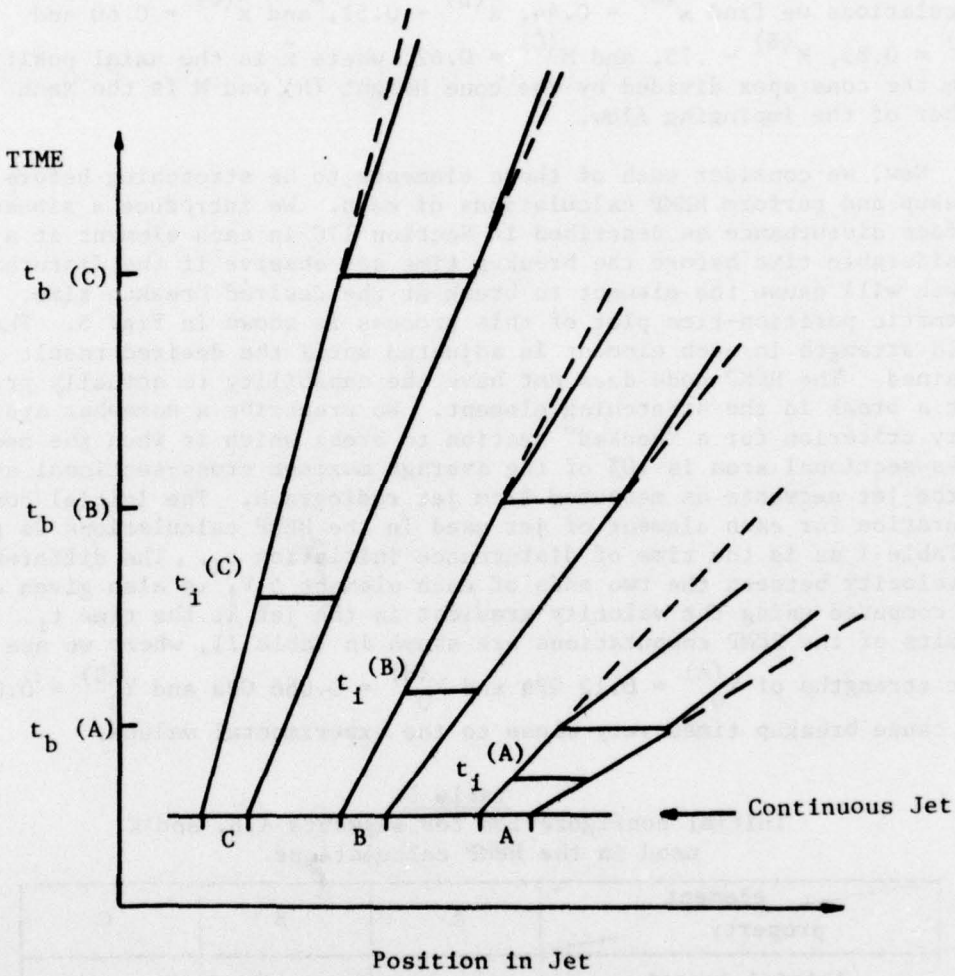

Figure 5. Schematic position-time plot showing elements A, B, and C used in HEMP calculations.

Table II

Results of HEMP calculations and comparison with experimental breakup time.

Element No.	x/h	M	Exp. b.u. time (μs)	HEMP	
				b.u. time (μs)	Yield Strn. (GPa)
A	.44	.85	94	94	0.12
B	.51	.75	121	119	0.066
C	.60	.62	161	159	0.036

2. Random Yield Strength

We have examined the effects of surface disturbance throughout our work so far. Suppose now we have no surface disturbance, but the yield strength of the material varies from cell to cell in the HEMP calculations. As before, we have used a portion of jet subject to a linear velocity gradient, which is shown in Fig. 6. Note that only the portion above the centerline is shown for convenience. The calculation grid is divided into 96 cells and the yield strengths of each cell are distributed randomly throughout the grid, assuming the following distribution:

No. of cells	Y_0 (GPa)
40	0.200
15	0.210
15	0.190
10	0.175
10	0.225
3	0.160
3	0.240

The initial dimensions and velocity gradient are chosen such that the portion of jet shown will be equal to two average segment lengths of jet at the breakup time, as measured from the radiographs. Figure 6 shows the configuration of the jet at 18 μs and 36 μs. It is interesting to note that it appears to break into two full segments plus a little extra. Thus we see that the HEMP calculation predicts segment length in the neighborhood of the measured lengths.

3. Details of the Stress Distribution in a Jet

In the Appendix to this report we have compiled for easy reference the stress distribution as predicted by HEMP for a stretching jet with a sinusoidal surface disturbance. The dimensions of the initial configuration are also given there. Tabular results are given

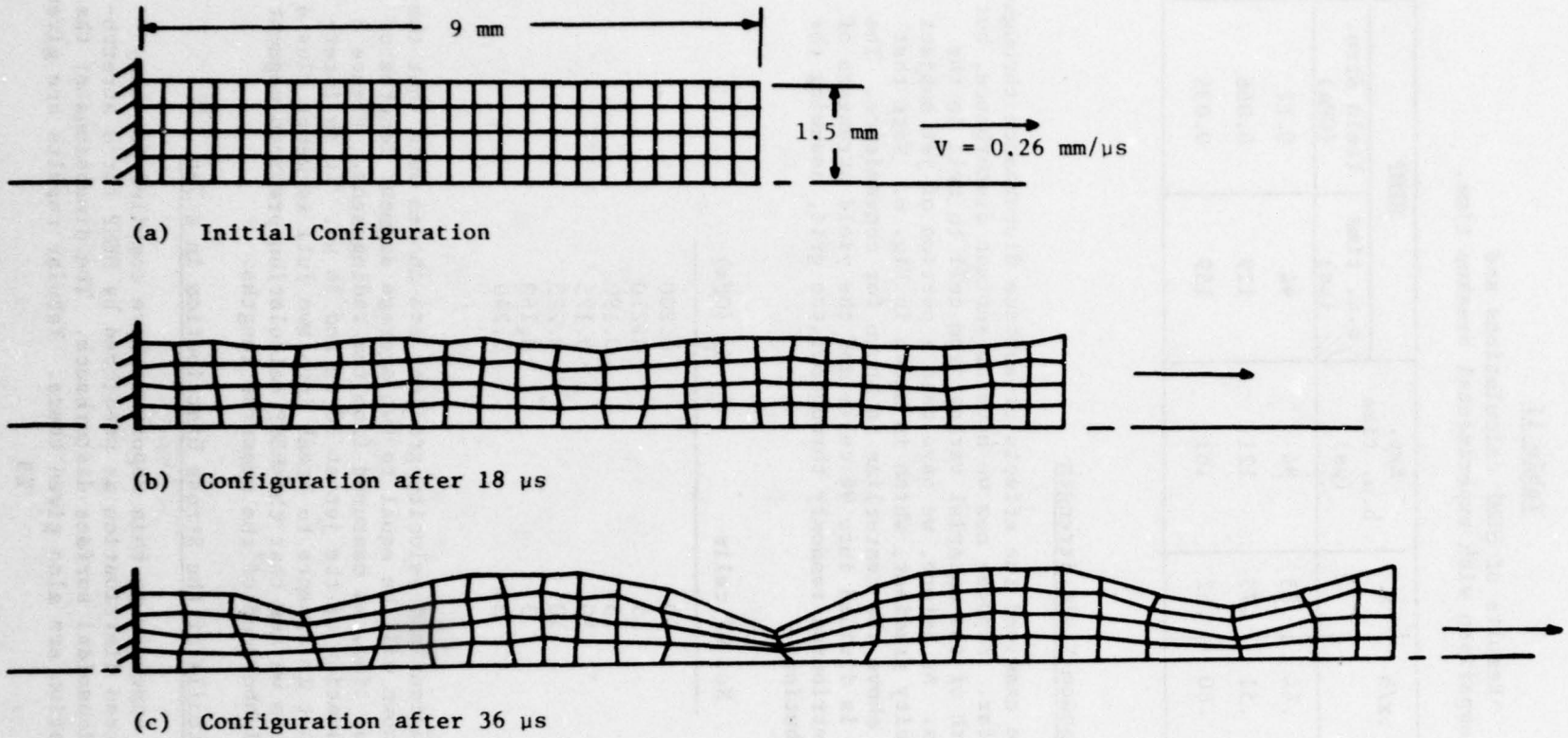

Figure 6. HEMP results of a jet with random yield strength distribution throughout.

at several times of interest and several plots of axial stress versus time are included. Note that the tabular data are given at very early times and at several times in the neighborhood of when the first appearance of elastic cells occurs. This was done to see the "start up" stress distribution as computed by HEMP. The later times were tabulated to observe the effects of the existence of elastic cells on the growth of the disturbance.

Finally, the stress time plots presented show that at early times the axial stress is somewhat erratic. In the necked region, we see that the cells remain plastic and the stress "levels off" at approximately the yield stress in simple tension, which indicates in this region the flow may be approximately one-dimensional. In the region away from the necked region we see that the cells eventually become elastic with a general decrease in the axial stress.

4. The Effect of Calculational Mesh Size

We have examined the effect of using fewer grid cells in the HEMP code calculations of a jet stability problem (since fewer cells will be more economical to calculate). In our typical calculations we have been using 5 cells across the radius of the jet and 16 cells along each disturbance wavelength. To observe the effect of mesh size, we have considered two problems which are identical except for the cell structure. One has the standard 5x16 structure whereas the other only has 2 cells across the radius and 6 cells along one disturbance wavelength. The relative growth of disturbance amplitude Δ, defined in Section IID is plotted versus time for each case on Fig. 7. We see that the case with fewer cells grows somewhat slower than the more accurate case, but it still shows the same basic trend. We may therefore use fewer cells when we are interested in the trends of a series of different problems. This will save computer time and enable us to study the results much sooner.

5. The Effect of Disturbance Amplitude

In our previous calculations, for the most part, the value of the amplitude of the initial disturbance has been taken as 5% of the initial jet radius. We next examine the case where the initial disturbance amplitude is much smaller, 0.1% of the initial radius. Figure 8 shows the results of a comparison between two identical calculations except for the amplitude of the disturbance. In Fig. 8, the minimum radius versus time is plotted for each case. We see that after a given amount of time, the case with the smaller initial amplitude does not neck down as much as the case with larger initial amplitude, but significant growth does occur. In fact, percentage wise, the growth for the smaller amplitude disturbance is somewhat larger as can be seen by computing the relative growth Δ. For example, at $t = 24\ \mu s$, Δ for the case with small amplitude is 4.3, whereas Δ for the case with large amplitude is 3.6. Recall that for the example in Section IID there was

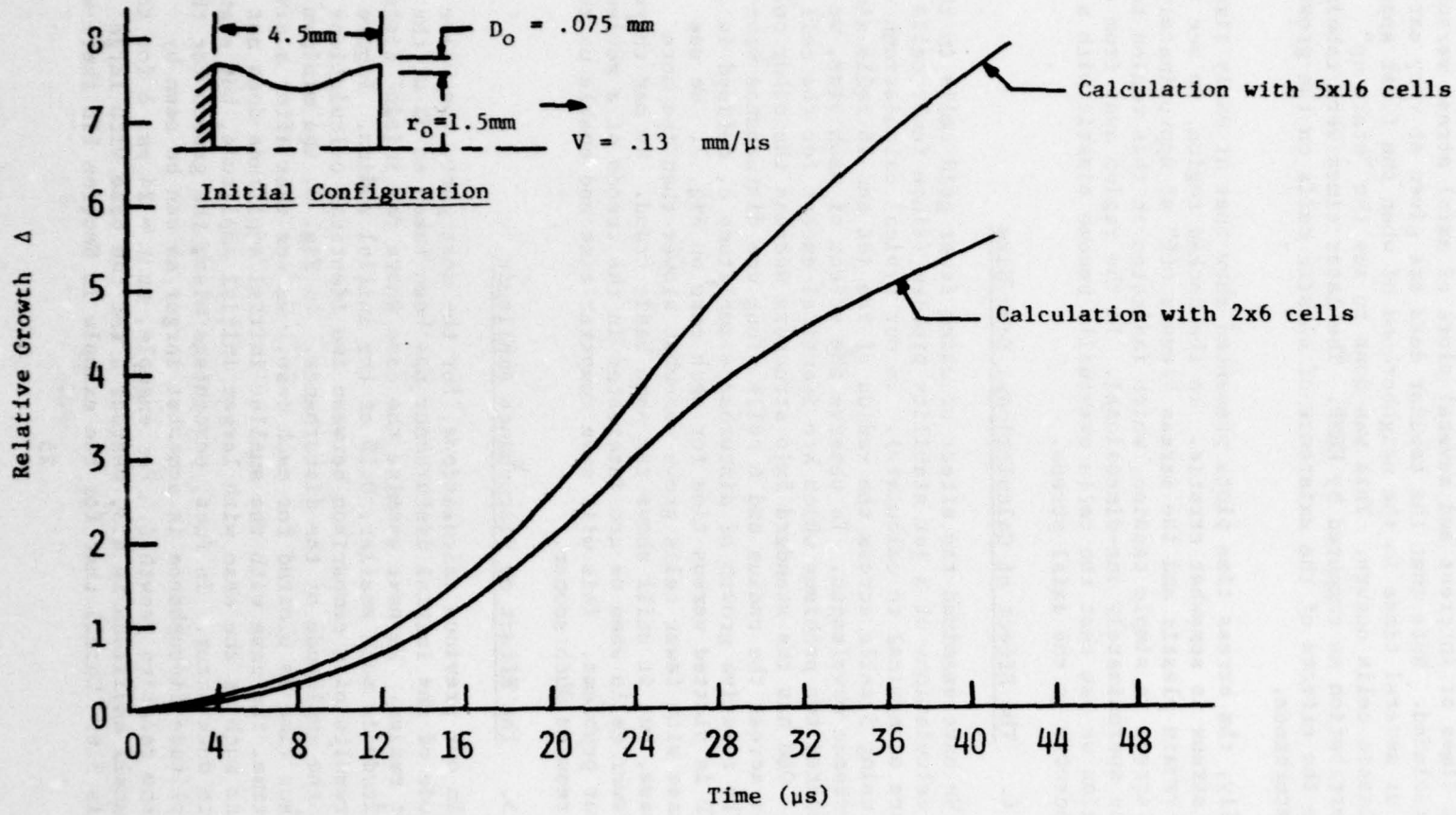

Figure 7. Comparison of HEMP calculations of a stretching jet with two different mesh sizes.

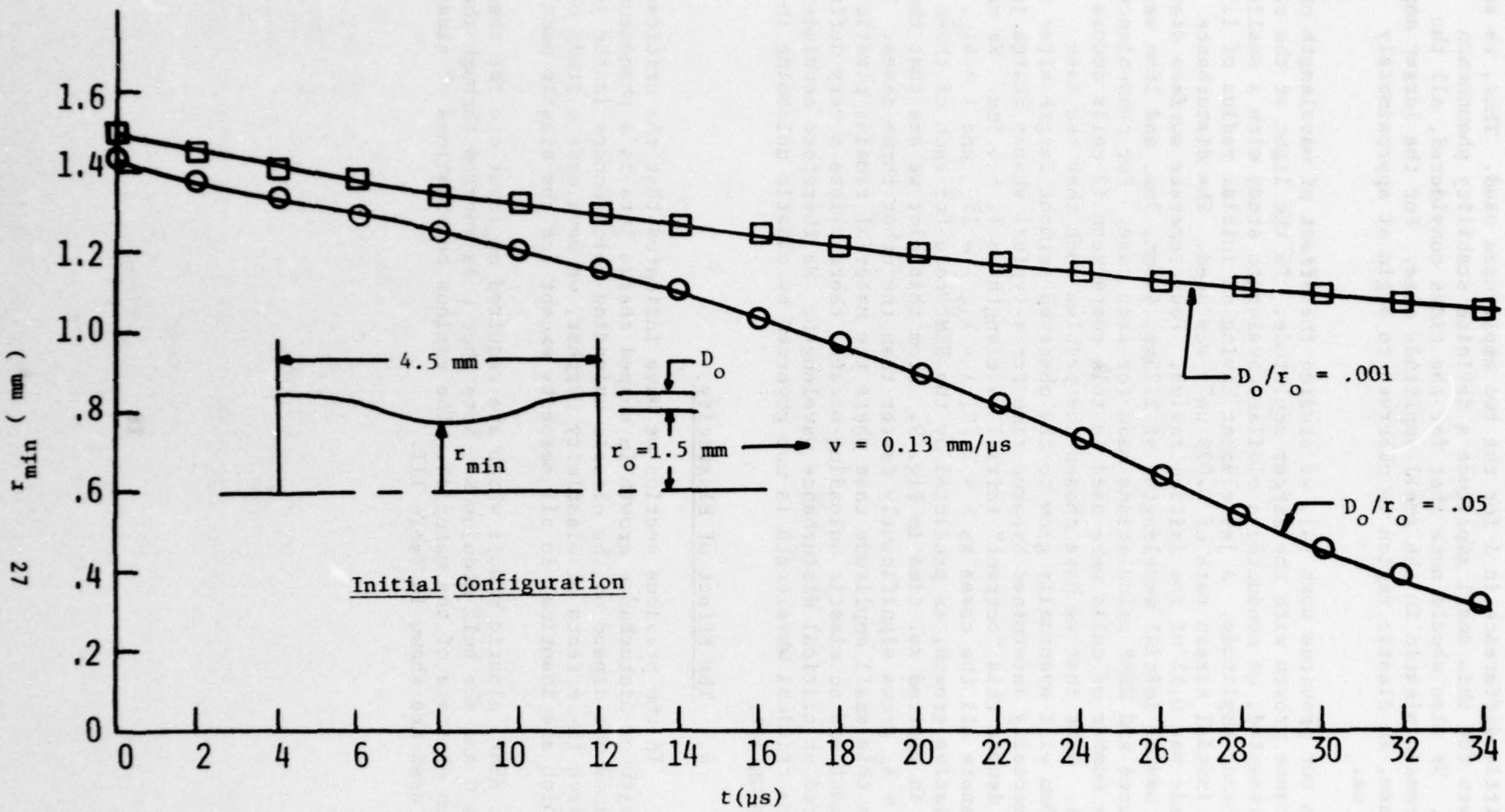

Figure 8. A comparison of minimum jet radius histories as predicted by HEMP for two jets with different initial disturbance amplitudes.

very little difference in Δ for the two amplitudes used. Thus, we see that even for this small amplitude a definite stability phenomenon occurs. We also should note that for the times considered, all the cells remain plastic in the small amplitude case. For the larger amplitude case, an elastic region is observed to begin at approximately $t = 12\ \mu s$.

In our previous work [4], we studied the effect of wavelength on disturbance growth with the larger amplitude. In the light of the results just presented, we conducted a similar wavelength study with a smaller disturbance amplitude. A jet element having an initial radius of 1.5mm and an initial strain rate of $0.029\ \mu s^{-1}$ was used. The disturbance amplitude was 0.1% of the initial radius. Four separate surface disturbances having initial wavelengths of 2.25mm, 4.5mm, 9mm, and 18mm were introduced and HEMP calculations made for each case. For convenience, a smaller number of cells were used in this comparison (2 cells across the radius). Note that we have chosen the problem such that the case $\lambda = 4.5$mm will eventually grow to the observed segment length after the experimentally determined breakup time for a typical shaped charge jet. Let us denote this "correct" initial wavelength as $\lambda_c = 4.5$mm. We can then denote all the cases as $\lambda = \lambda_c/2$, $\lambda = \lambda_c$, $\lambda = 2\lambda_c$, and $\lambda = 4\lambda_c$. The relative growth, as predicted by the HEMP code for each of these cases, is plotted vs. time in Fig. 9. From this plot we see that the case $\lambda = \lambda_c$ grows significantly faster than the other three cases. Thus, even in this small amplitude case where the material remains plastic throughout and no elastic unloading occurs, there exists a very definite preferred or critical disturbance wavelength. We therefore conclude that the critical wavelength is not governed by elastic unloading in the stretching jet.

6. The Effect of Elasticity

In the previous section we have indicated that the critical wavelength of disturbance growth in shaped charge jets is a phenomenon which does not depend on the elastic unloading which occurs in the jet. To observe the effects of elasticity further, we have made a study of jets which are identical in all respects except for the elastic moduli.

In HEMP, elastic moduli which are required as input are the shear modulus G and the bulk modulus K. Note that K is entered through the equation of state of the material. The various combinations of elastic moduli used are shown in Table III.

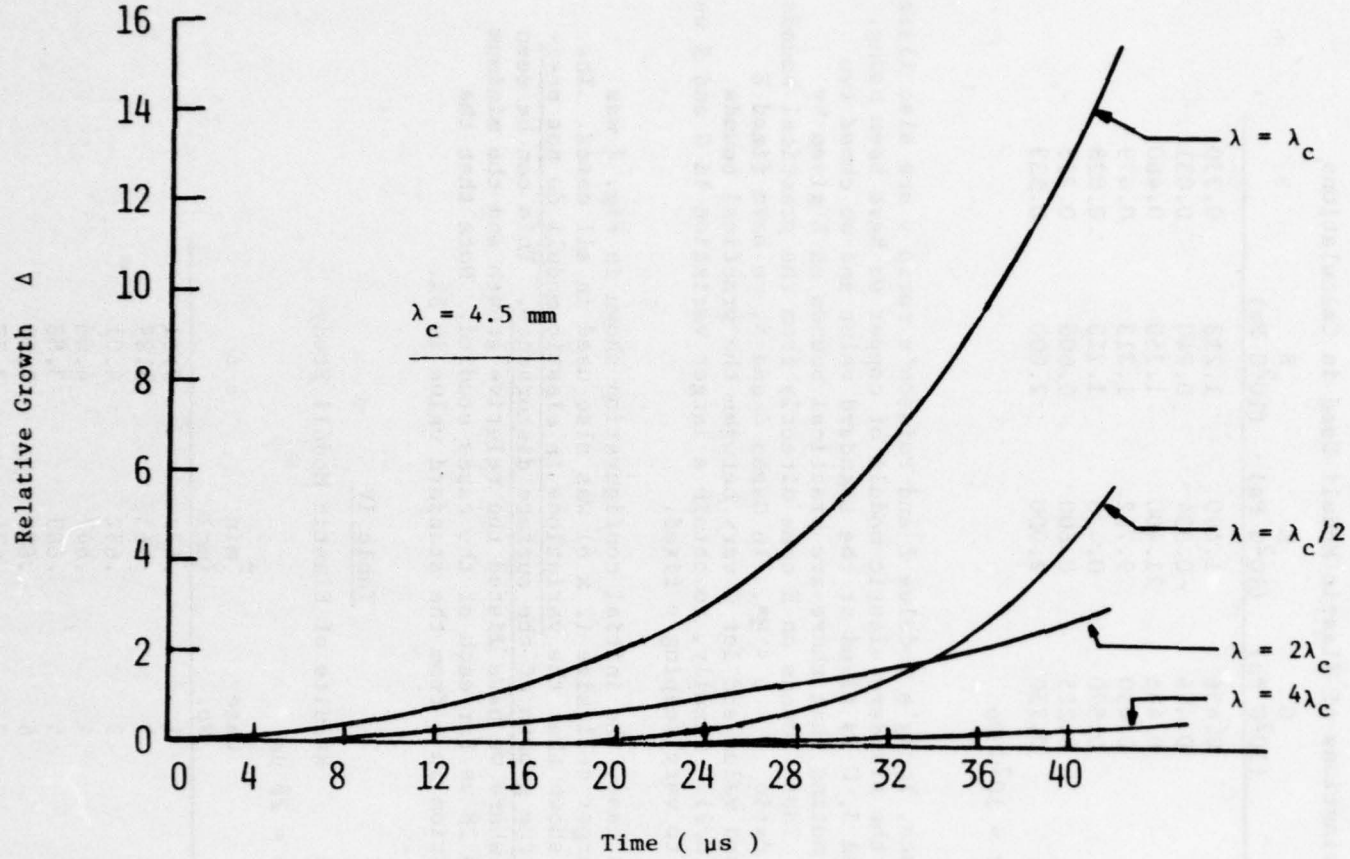

Figure 9. Relative growth vs. time for surface disturbances of four different wavelengths. In all cases, the jets have the same radius and strain rate.

Table III

Combinations of Elastic Moduli Used in Calculations

Case No.	G (10^2G Pa)	K (10^2G Pa)	E (10^2G Pa)	ν
1	0.456	1.190	1.213	0.330
2	0.456	0.334	0.940	0.031
3	0.456	11.400	1.350	0.480
4	0.410	9.752	1.213	0.479
5	0.590	0.428	1.213	0.028
6	0.225	0.600	0.600	0.333
7	0.750	2.000	2.000	0.333

Note: 1 M bar = 10^2G Pa

For convenience, Young's modulus E and Poisson's ratio ν are also listed. Case 1 gives the standard elastic moduli of copper we have been using. In Cases 2 and 3, G is fixed at the standard value and we chose two values for E noting that there are practical bounds on E given by $2G < E < 3G$. These bounds on E come directly from the practical bounds on Poisson's ratio $0 < \nu < \frac{1}{2}$*. In Cases 4 and 5, we have fixed E at the standard value and let G vary between the practical bounds $(E/3) < G < (E/2)$. Finally, to obtain a larger variation in G and E we allowed both to vary keeping ν fixed.

For each case, the initial configuration shown in Fig. 7 was used. The larger cell size (2 x 6) was also used in all cases. The results have shown that the variations in elastic moduli do not seriously affect the growth of the surface disturbance. This can be seen in Table IV, where we have listed the relative growth and the minimum radius at t = 28 μs for each of the cases studied. Note that the largest devistion in Δ from the standard value is 5%.

Table IV

Results of Elastic Moduli Study

t = 28 μs

Case No.	r_{min} (mm)	Δ
1	.672	3.81
2	.663	3.89
3	.652	4.01
4	.647	4.06
5	.663	3.88
6	.663	3.90
7	.676	3.77

* Note theoretically $-\frac{1}{2} < \nu < \frac{1}{2}$; however, no real materials have been found with $\nu < 0$, therefore we impose practical bounds of $0 < \nu < \frac{1}{2}$.

III. TWO-DIMENSIONAL CALCULATIONS OF MULTIPLE INTERIOR IMPACT PENETRATION

Another topic examined under the present study is the penetration of broken shaped charge jets. The object of this portion of the study is to define the mechanisms which cause the decrease in penetration associated with the increase in the gap between jet particles as experimentally observed in [8].

A. Background

Under a recent program conducted at Drexel University [7-10], experiments were performed which studied the effects of projectiles impacting upon the bottom of a pre-drilled hole in a target. We define the term "multiple interior impact" to describe this general setup. These tests were designed to simulate penetration by a segmented shaped charge jet. In these experiments, two low speed (approximately 1mm/μs) lead projectiles, separated by a pre-determined gap, were impacted upon soft homogeneous lead targets. It was concluded from these experiments that a definite relationship exists between the size of the gap and total penetration. As the gap between projectiles increases, total penetration, in general, decreases. The probable cause for this decrease was attributed to the interference between the trailing projectile and the occlusion or "back flow" caused by the leading projectile. This interference causes the formation of three distinct cavities in the target as shown in [8-10]. It is likely that this interference mechanism is the cause of the "scalloped" hole observed from the penetration of broken shaped charge jets (see [29]).

During the present study we conducted two-dimensional HELP code calculations to gain an understanding of the multiple interior impact process. In our first series of calculations we used lead projectiles at low speeds, impacting lead targets to simulate experiments in [8-10]. We also computed copper projectiles, having dimensions of typical shaped charge jet segments, impacting at typical shaped charge jet velocities onto steel targets.

B. General Approach

The HELP code [11] was used for all the multiple interior impact calculations. This two-dimensional finite-difference code uses a combined Eulerian-Lagrangian hydrodynamic method which treats multi-material problems with a continuous description of the moving mass. The method used in HELP handles material interfaces and free surfaces by propagating these surfaces as sharp Lagrangian discontinuities through the stationary Eulerian grid. This code has the capability of treating elastic and plastic effects.

The version of HELP used did not have the necessary routines to set up the target and projectile shapes used in the Drexel experiments [8-10].

Therefore an auxiliary set up package, known as HELPCLAM [30], obtained through the courtesy of John Harrison, BRL, was used to set up the necessary geometries. The original projectiles were modeled as cylinders or cylinders with conical tips. An example of the computational grid and a typical initial configuration used for these problems are shown in Figures 10 and 11 respectively. Table V summarizes the initial conditions for the four configurations studied.

The Tillotson equation of state, as specified in the HELP code [10] for each of the materials considered, was used.

C. Impact of Lead Projectiles on Lead Targets

We have computed three separate configurations of low speed (≅ 1mm/μsec) multiple interior impact problems using projectiles and targets made of lead. The first calculation (Table V, No. 1), simulated one of the experiments presented in [9]. Figure 11 shows the initial configuration for this problem. The initial gap between projectiles is approximately 22mm. The yield strength for lead was chosen to be 6.89 MPa.

Table V

Summary of the initial conditions of the HELP Code Calculations

Run No.	Projectile	Projectile yield strength (Pa)	Gap (mm)	Target	Target yield strength (Pa)
1	Lead	6.89×10^6	22	Lead	6.89×10^6
2	Lead	6.89×10^6	37	Lead	2.756×10^6
3	Lead	6.89×10^6	37	Lead	2.756×10^5
4	Copper	6.89×10^7	14	Steel	2.41×10^8

Figures 12 through 16 show the computed projectile penetration at successive times after impact. Notice that these computer simulations show no interference between the trailing projectile and the target "back flow" caused by the first projectile. Thus, the computer simulation does not show the formation of the three distinct cavities observed in the experiments of [9].

A plot of computed depth of penetration vs. time after impact is given in Figure 17. The total penetration depth measured for the comparable experiment [9] is approximately 42mm. As one can see the HELP predicted penetration is only about one-half of the experimental value.

Though no interference was predicted in these calculations, the portion of the target directly parallel to the target hole axis moves

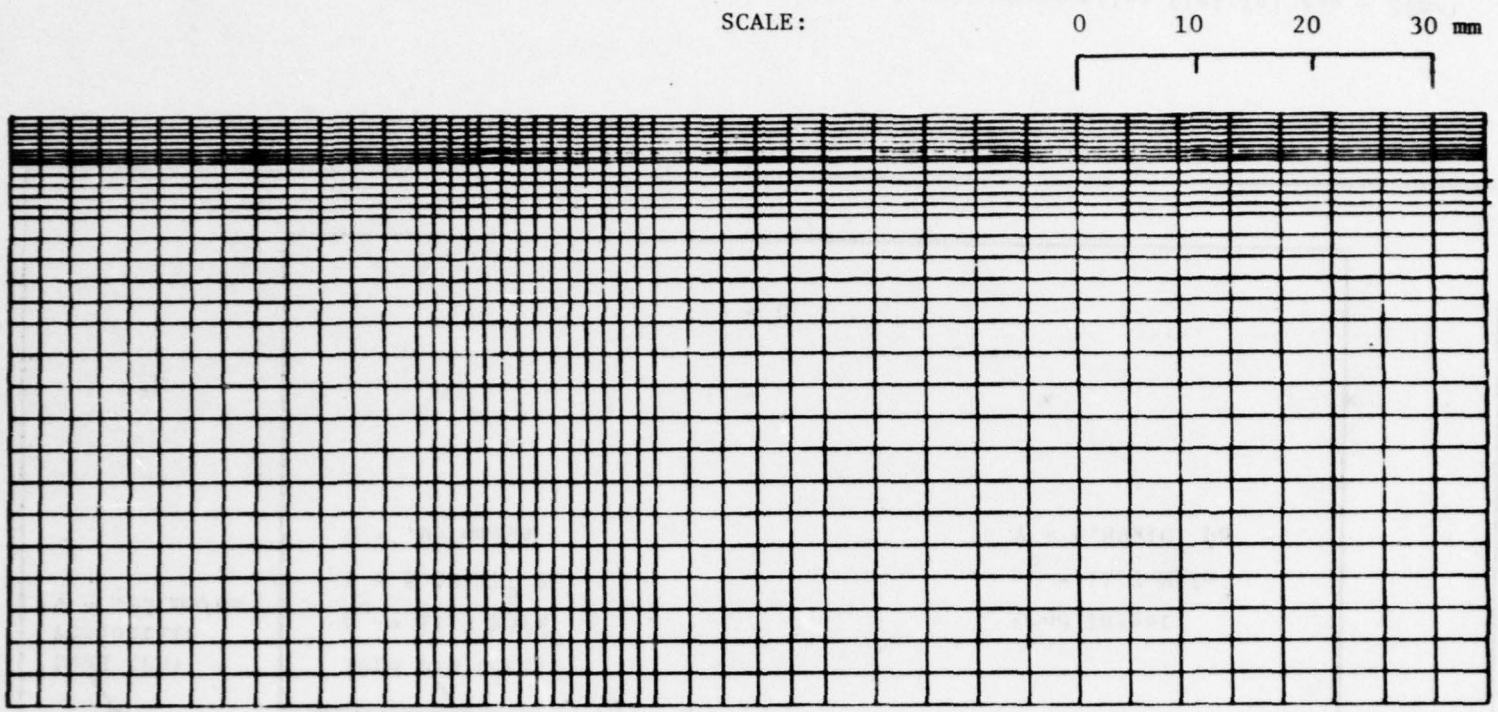

Figure 10. Example of the computational grid used in the HELP code calculations of the multiple interior impact problems.

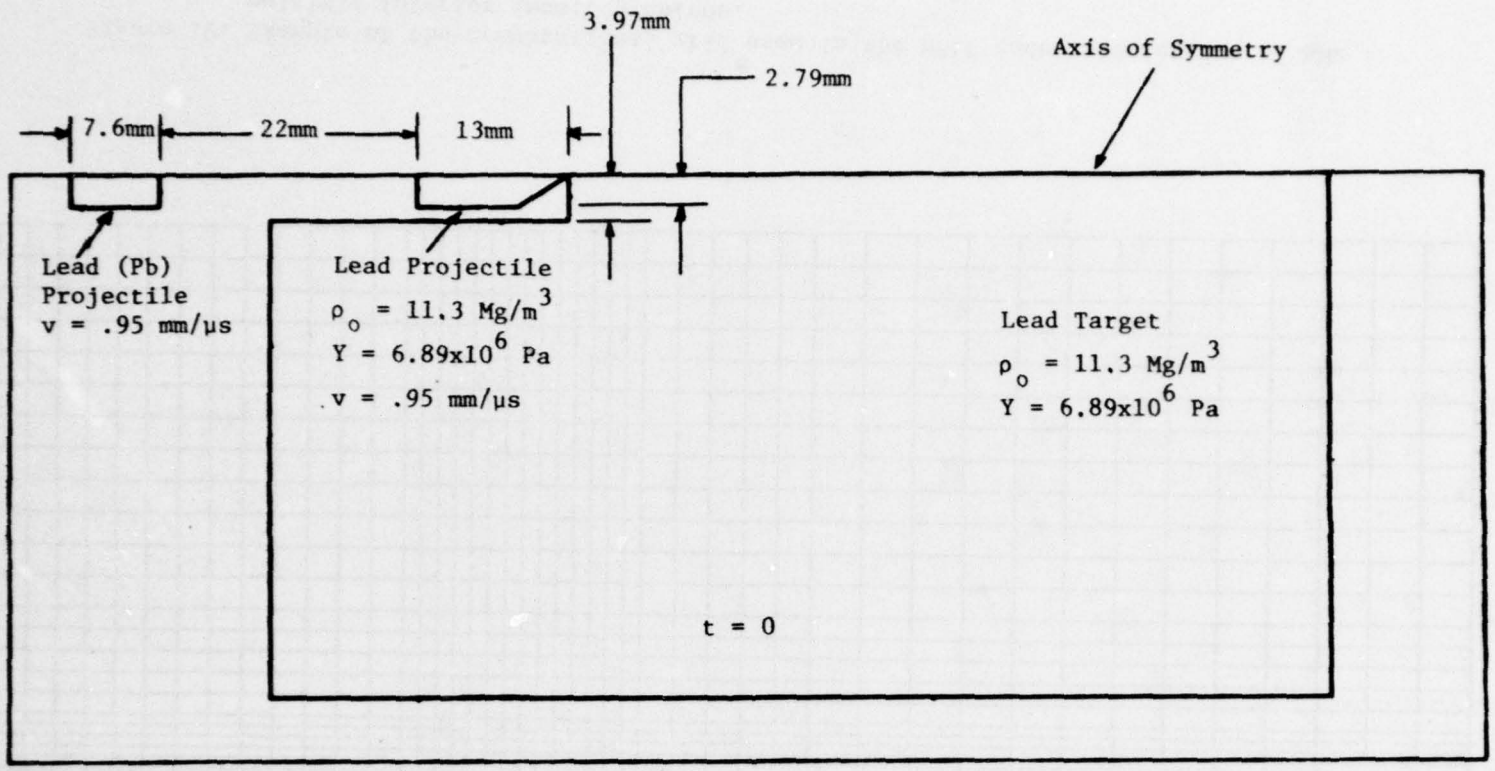

Figure 11. Initial configuration of the interior impact of lead projectiles (initial gap = 22mm) onto a lead target.

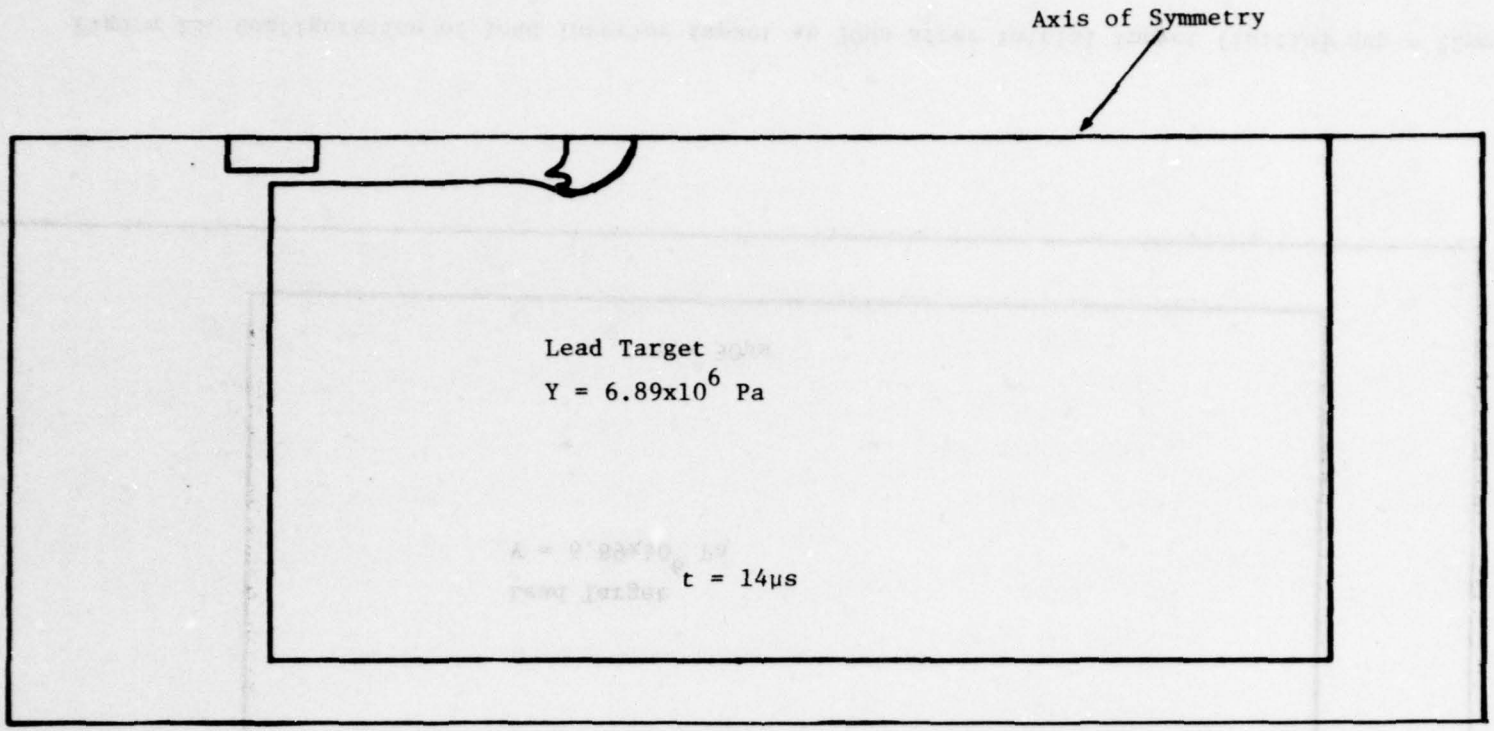

Figure 12. Configuration of lead interior impact (initial gap = 22mm) at 14μs after initial impact as predicted by HELP code.

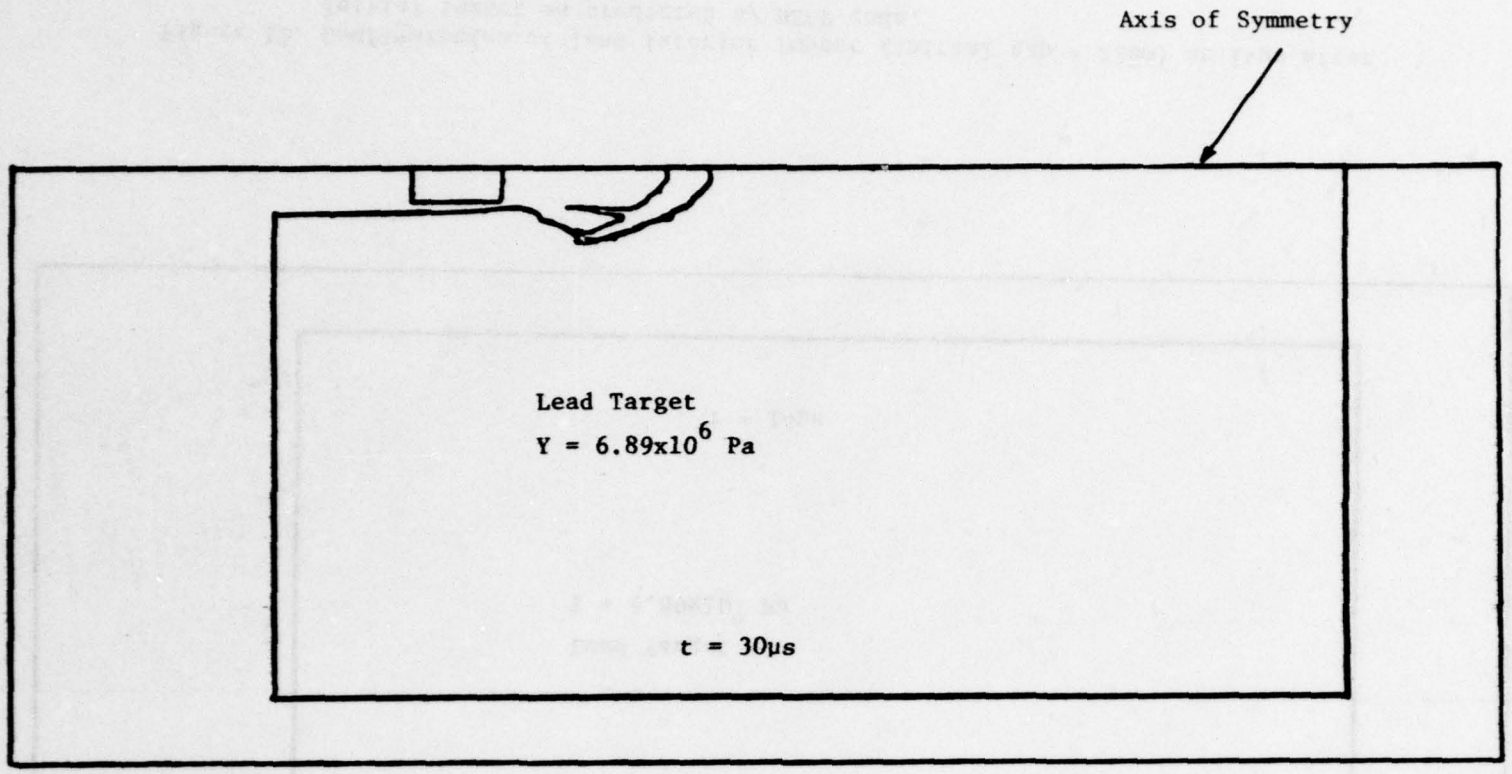

Figure 13. Configuration of lead interior impact at 30μs after initial impact (initial gap = 22mm).

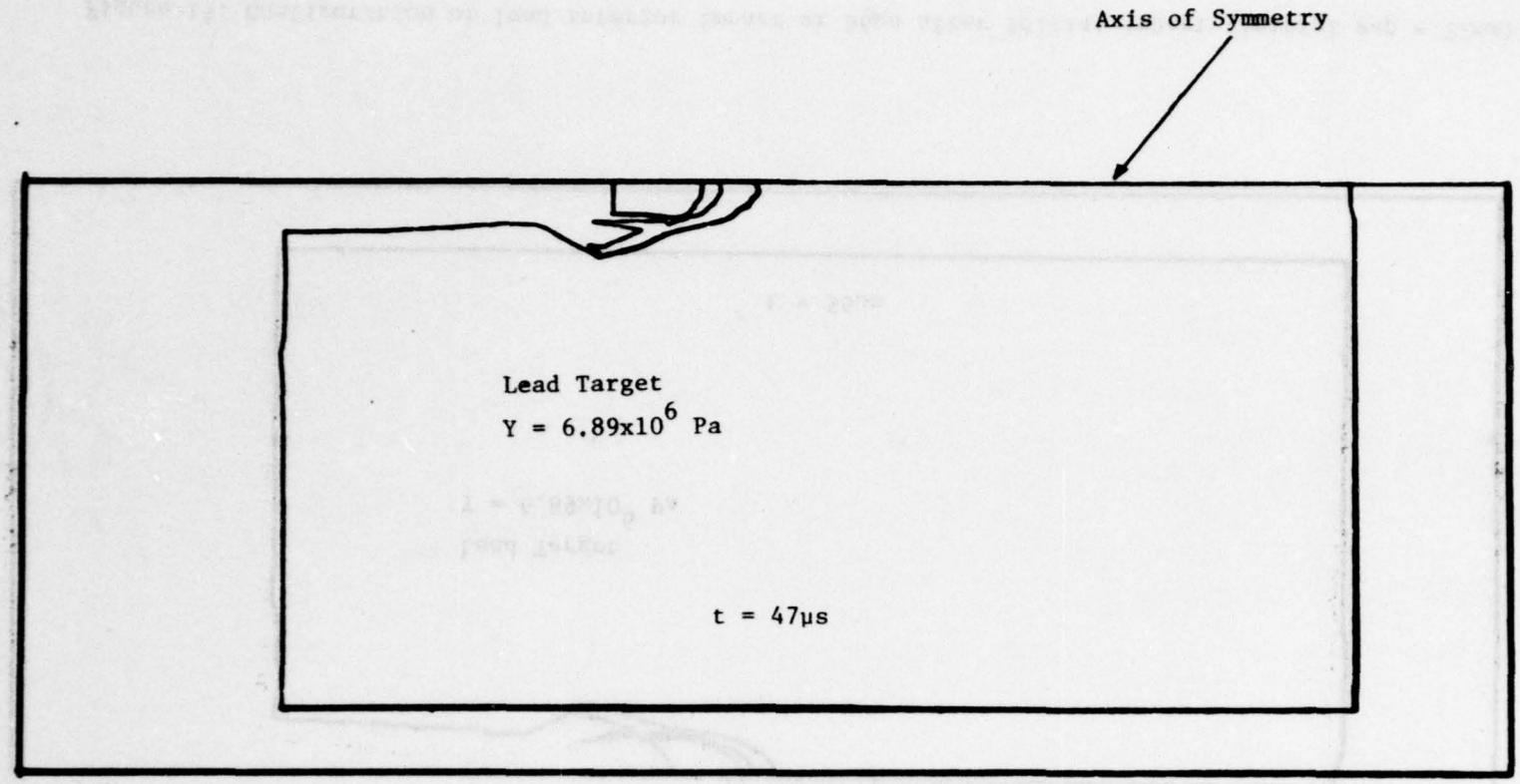

Figure 14. Configuration of lead interior impact at 47μs after initial impact (initial gap = 22mm).

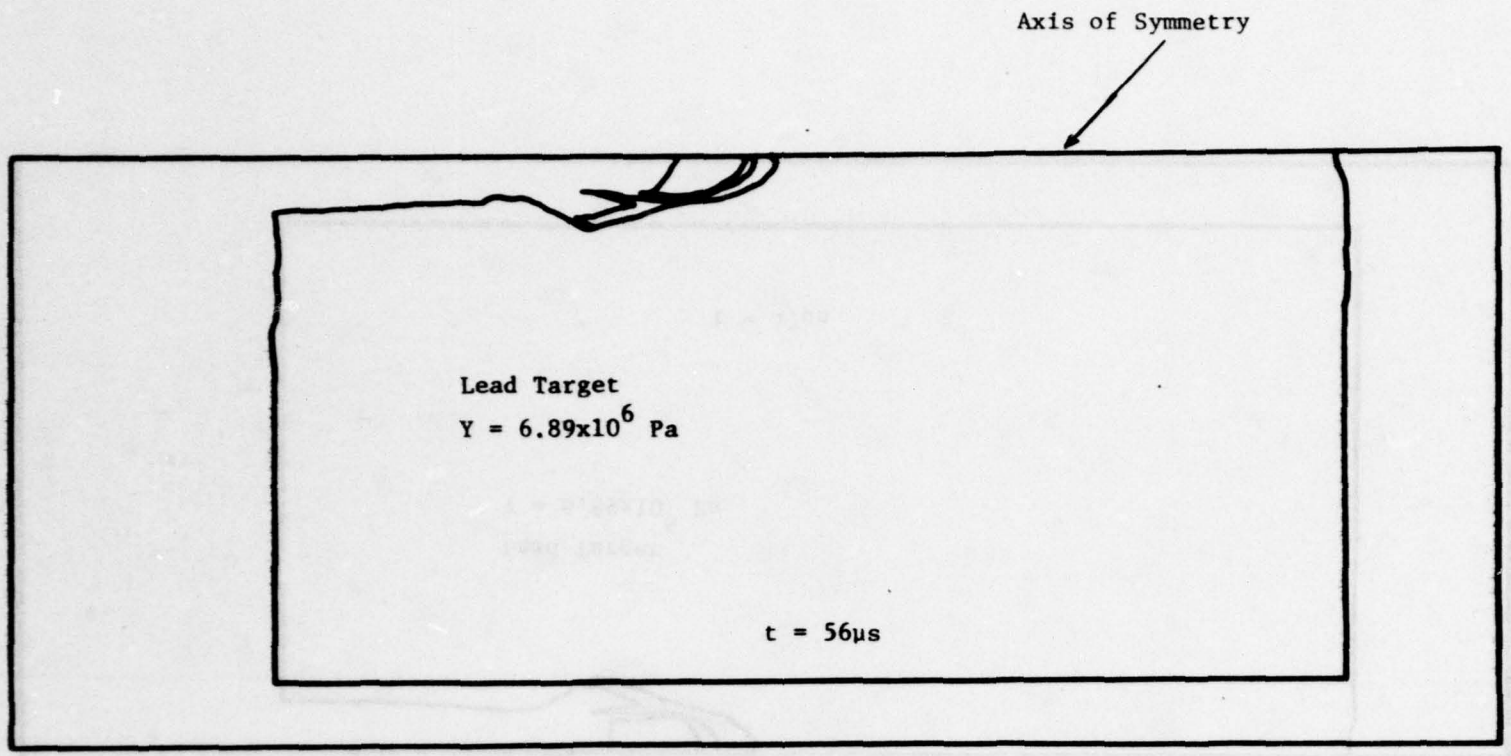

Figure 15. Configuration of lead interior impact at 56μs after initial impact (initial gap = 22mm).

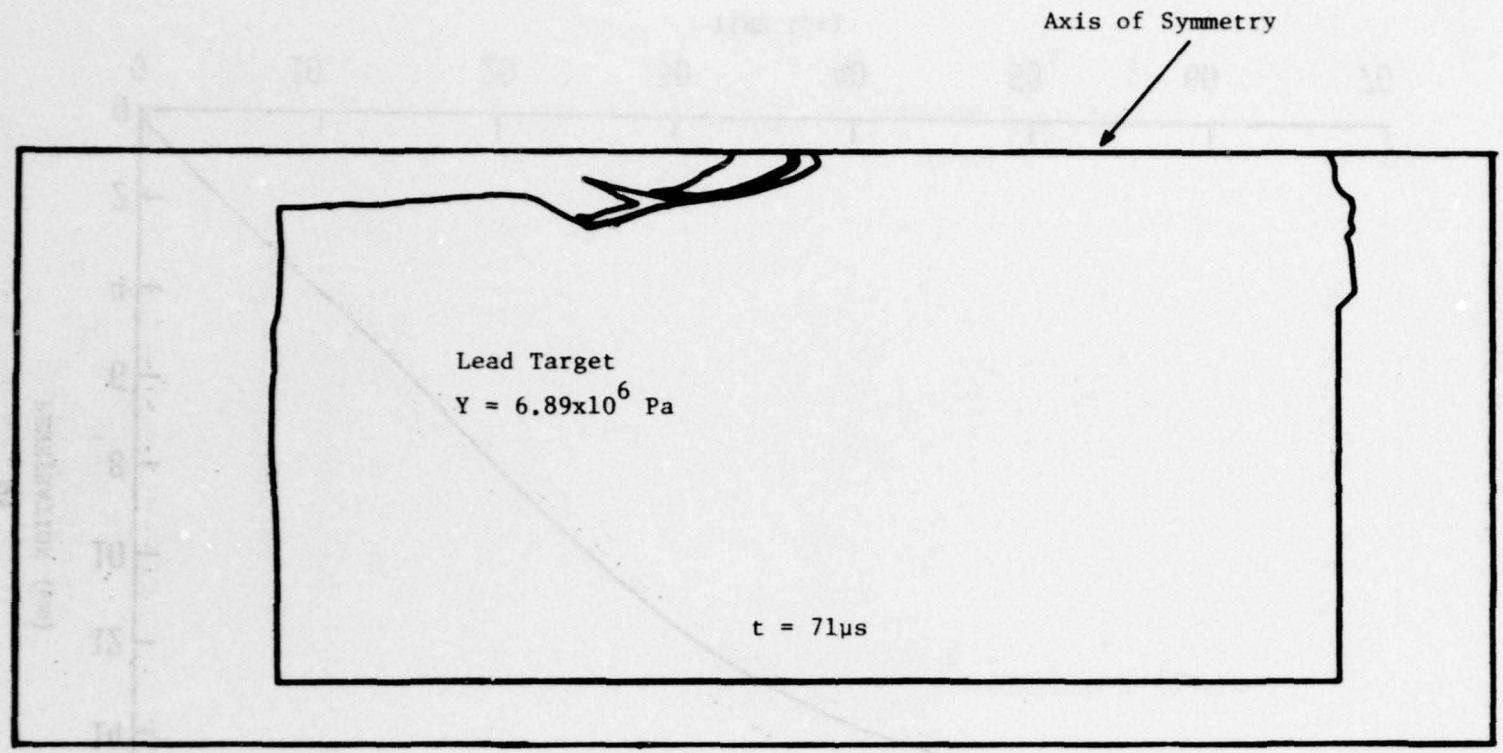

Figure 16. Configuration of lead interior impact at 71μs after initial impact (initial gap = 22mm).

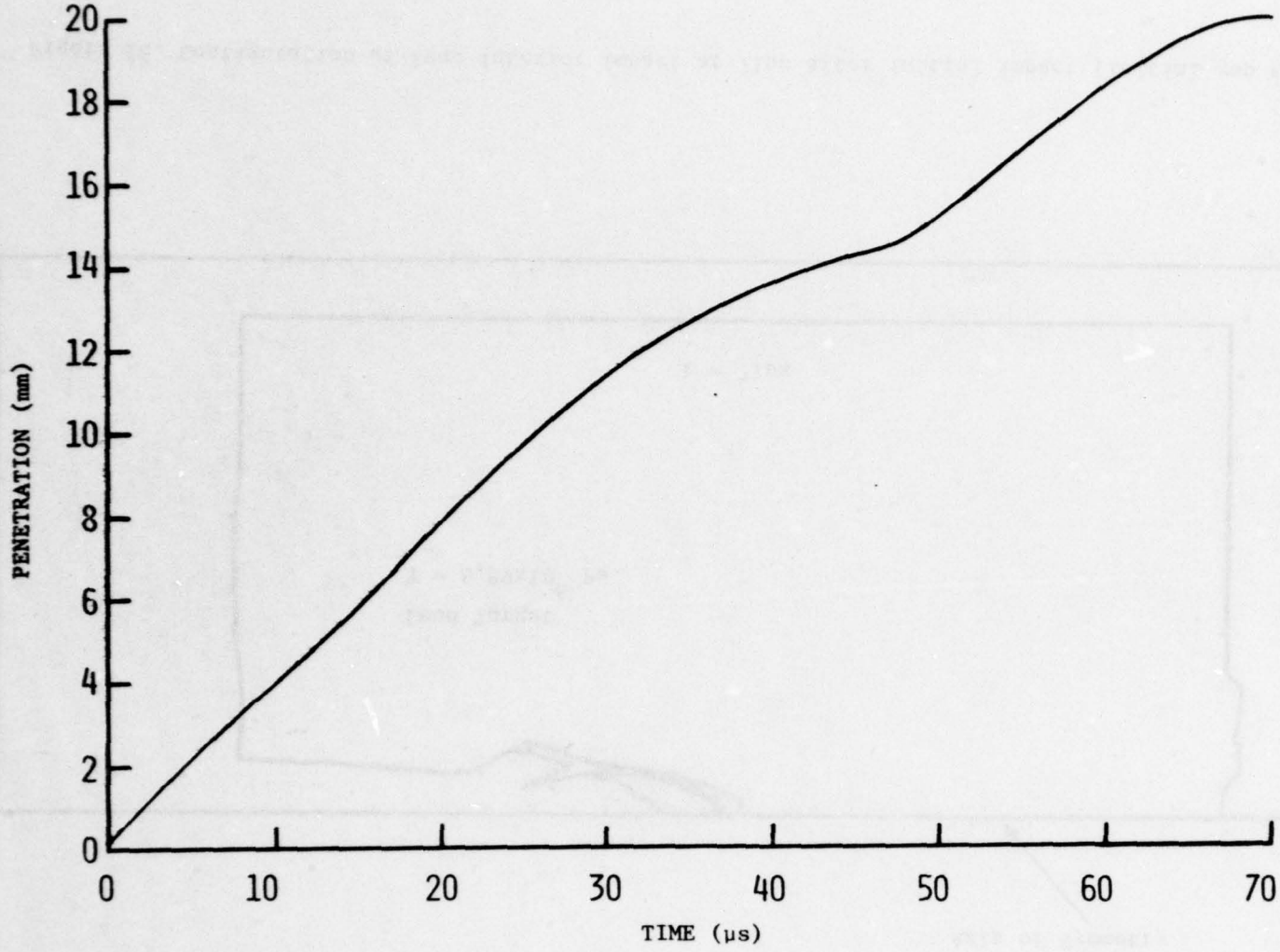

Figure 17. Penetration depth vs. time after initial impact as predicted by HELP for the interior impact of lead projectiles onto a lead target (initial gap = 22mm).

radially inward as can be seen in Figures 12 through 16. If the gap between projectiles were increased, this region of the target would have more time to move radially inward to a position where it would interfere with the path of the trailing projectile. Therefore, a second run was made, this time modeling an experiment with a larger spacing between projectiles.

This calculation (Table V, No.2) simulates one of the experiments reported in [8]. The initial gap between projectiles was approximately 37mm. From the discrepancy observed in the total penetration of the previous case, we felt that the lead was not being modelled properly in the code. The yield strength of the lead target was thus lowered to 2.76×10^6 Pa in an attempt to alleviate this problem. These and all other important dimensions are given in Figure 18.

Figures 19 through 21 show the calculated penetration at successive times after impact. From these computer simulations we have calculated that there is not enough time for the target "back flow" to move radially inward and interfere with the trailing projectile.

In the next run (Table V, No.3), the target yield strength was lowered by a factor of ten, to 2.76×10^5 Pa and computations were made. All other initial conditions were the same, as indicated in Figure 18. Figures 22 through 24 are the computer simulations of this run at successive times after impact. Again the radial velocity calculations indicate that no interference will occur between the trailing projectile and the target.

At 24 μsec after the initial impact the calculated penetration was 10.38 mm as compared to 9.42 mm penetration for the previous case (Table V, No.2). This increase in penetration is not substantial considering the 90% decrease in target yield strength.

The HELP code calculations did not compare well with the experimental results of [8] and [9]. The computed penetration was only about one-half of that measured. The code did not predict interference between the trailing projectile and the occlusion caused by the impact of the first, and thus the subsequent triple cavity in the target was not observed. One possible explanation for these computations being unsuccessful is the anomalous behavior of lead or, more appropriately, the lead equation of state used in the code.

D. Impact of Copper Projectiles on Steel Targets

In an attempt to understand the mechanism of this gap effect between projectiles, the HELP code was used to calculate the interior impact of two copper projectiles on a steel target. The dimensions of the copper projectiles were chosen to simulate typical jet segments of an 81.3 mm BRL charge. These dimensions, along with those of the target, are given in Figure 25. Figures 26 and 27 are the computer simulations of this run at 4 and 9 μsec after impact respectively.

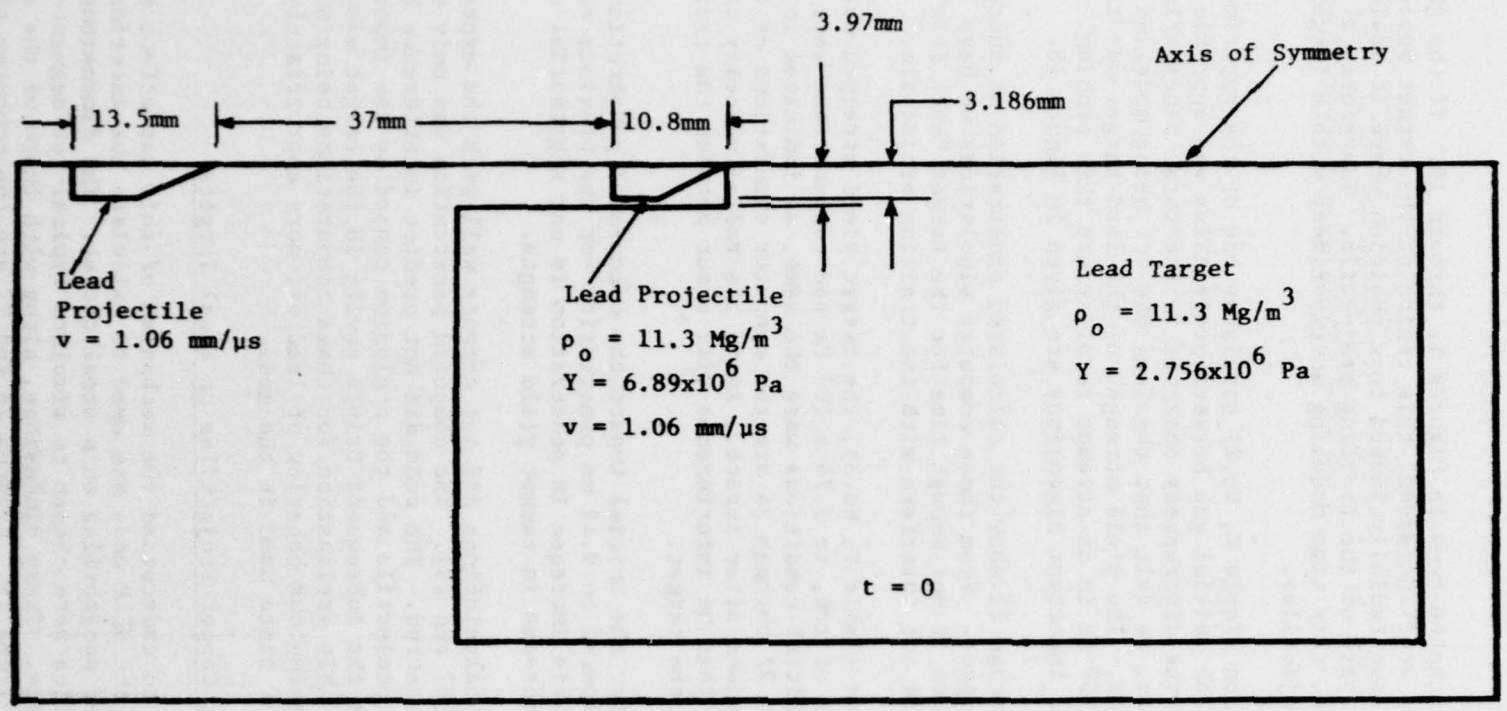

Figure 18. Initial configuration of the interior impact of lead projectiles (gap = 37mm) onto a lead target.

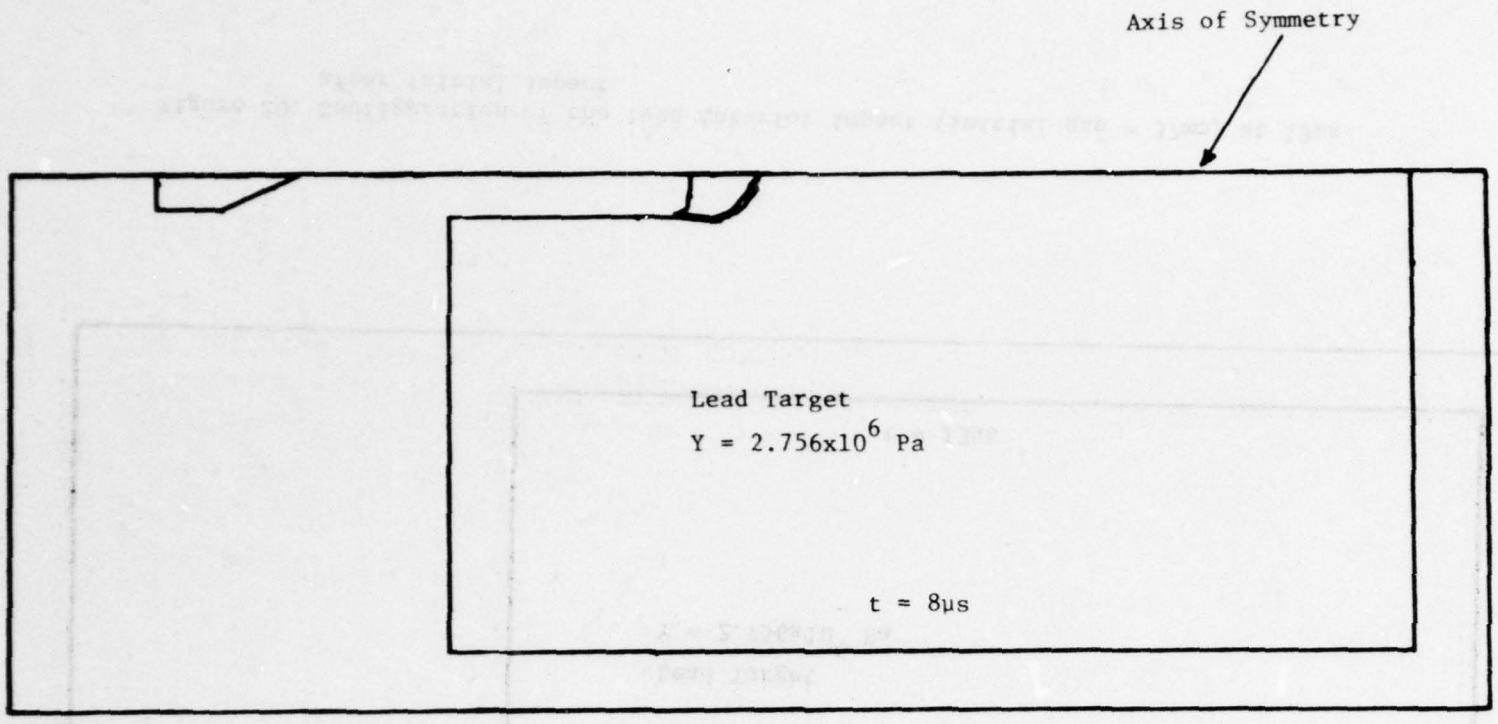

Figure 19. Configuration of the lead interior impact (initial gap = 37mm) at 8μs after initial impact as predicted by HELP code.

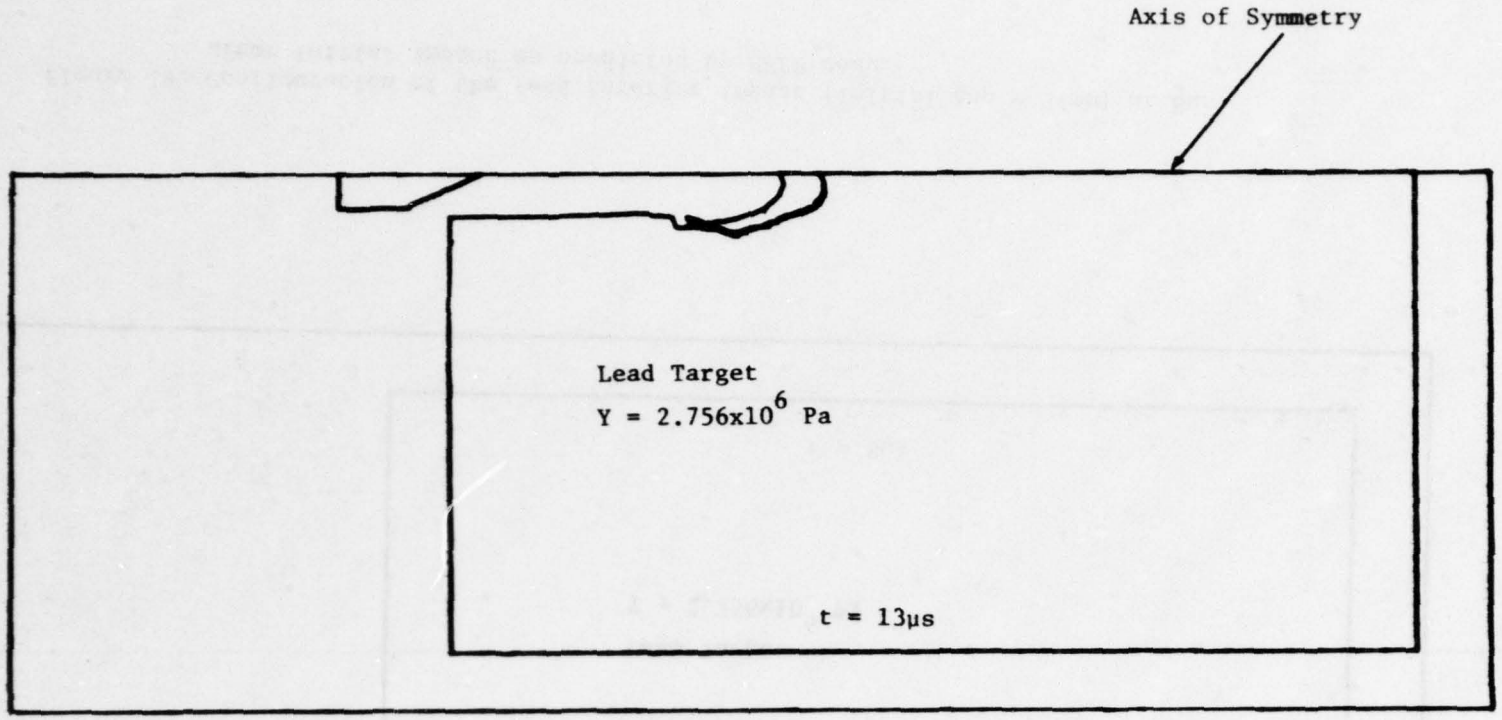

Figure 20. Configuration of the lead interior impact (initial gap = 37mm) at 13μs after initial impact.

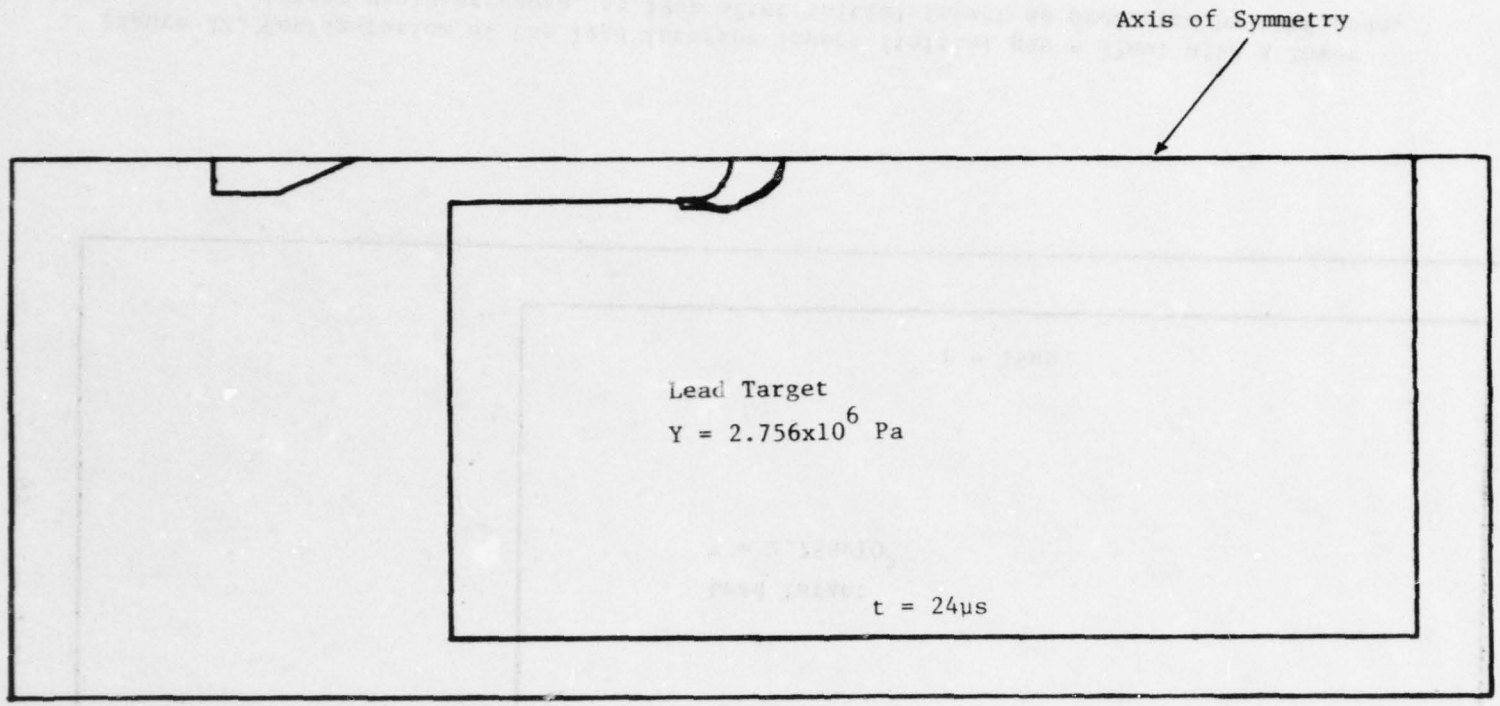

Figure 21. Configuration of the lead interior impact (initial gap = 37mm) at 24μs after initial impact.

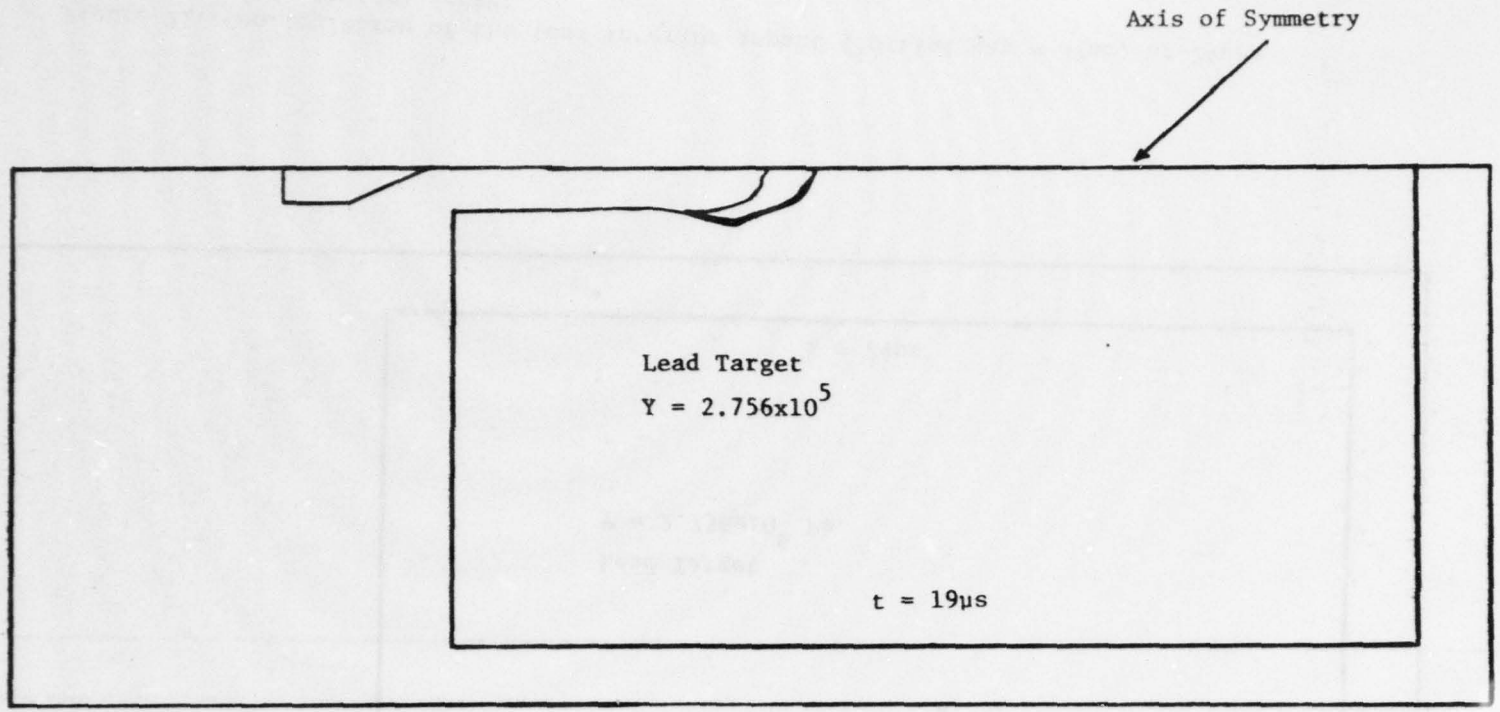

Figure 22. Configuration of the lead interior impact (initial gap = 37mm) with a lower target yield strength, at 19μs after initial impact as predicted by HELP code.

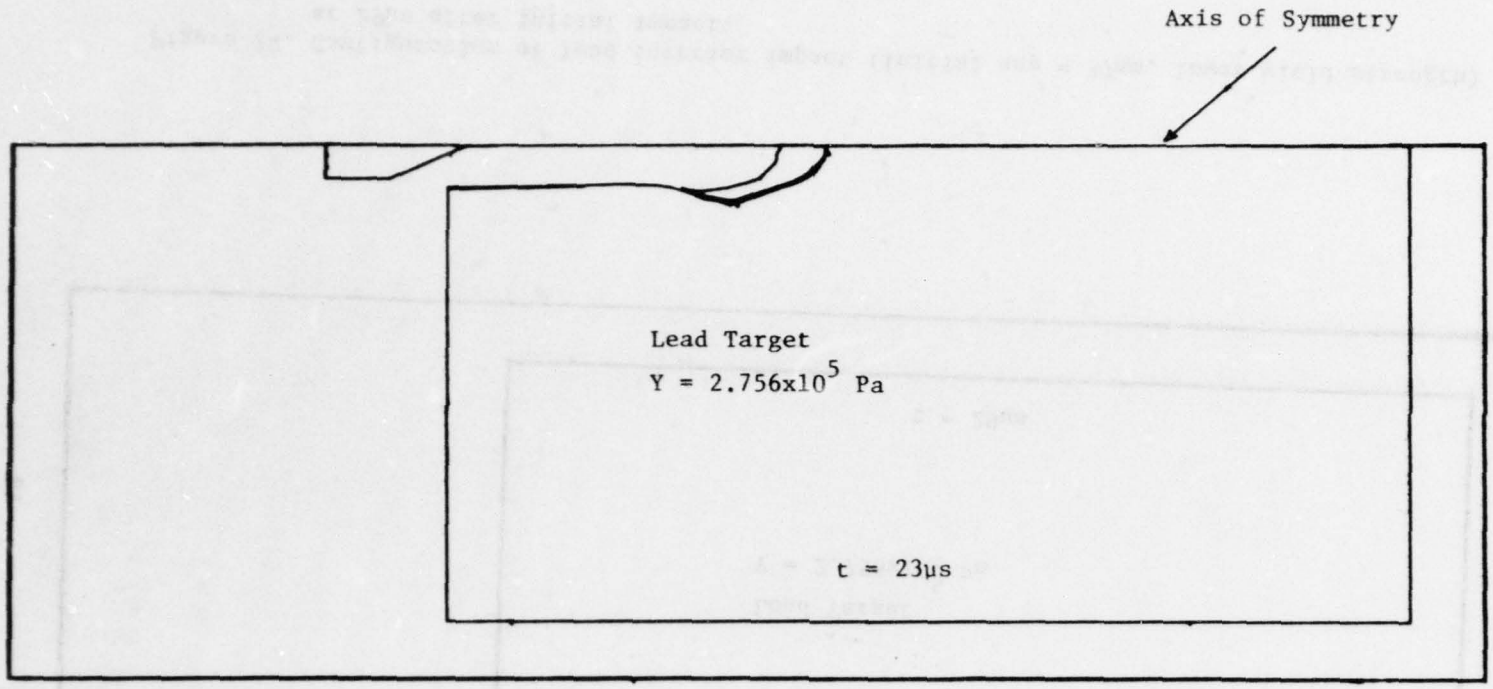

Figure 23. Configuration of lead interior impact (initial gap = 37mm, lower yield strength) at 23μs after initial impact.

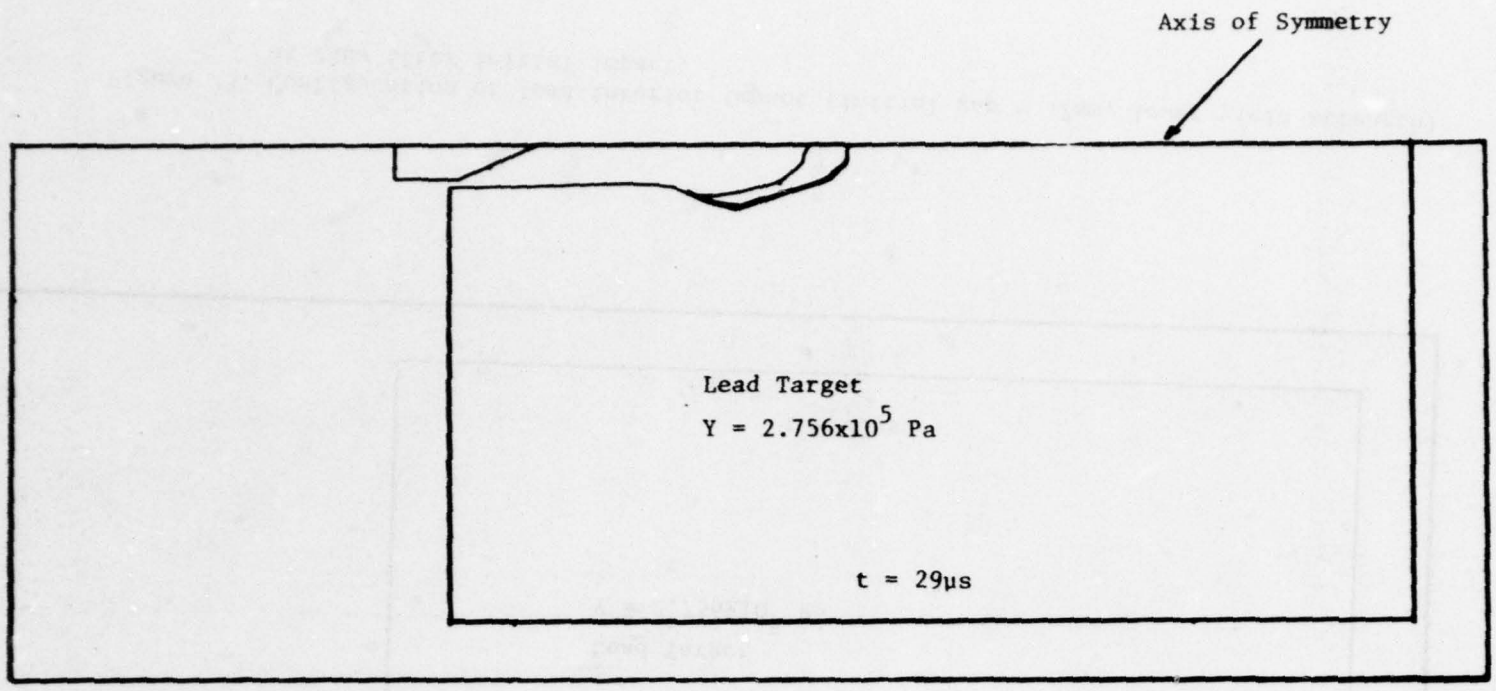

Figure 24. Configuration of lead interior impact (initial gap = 37mm, lower yield strength) at 29μs after initial impact.

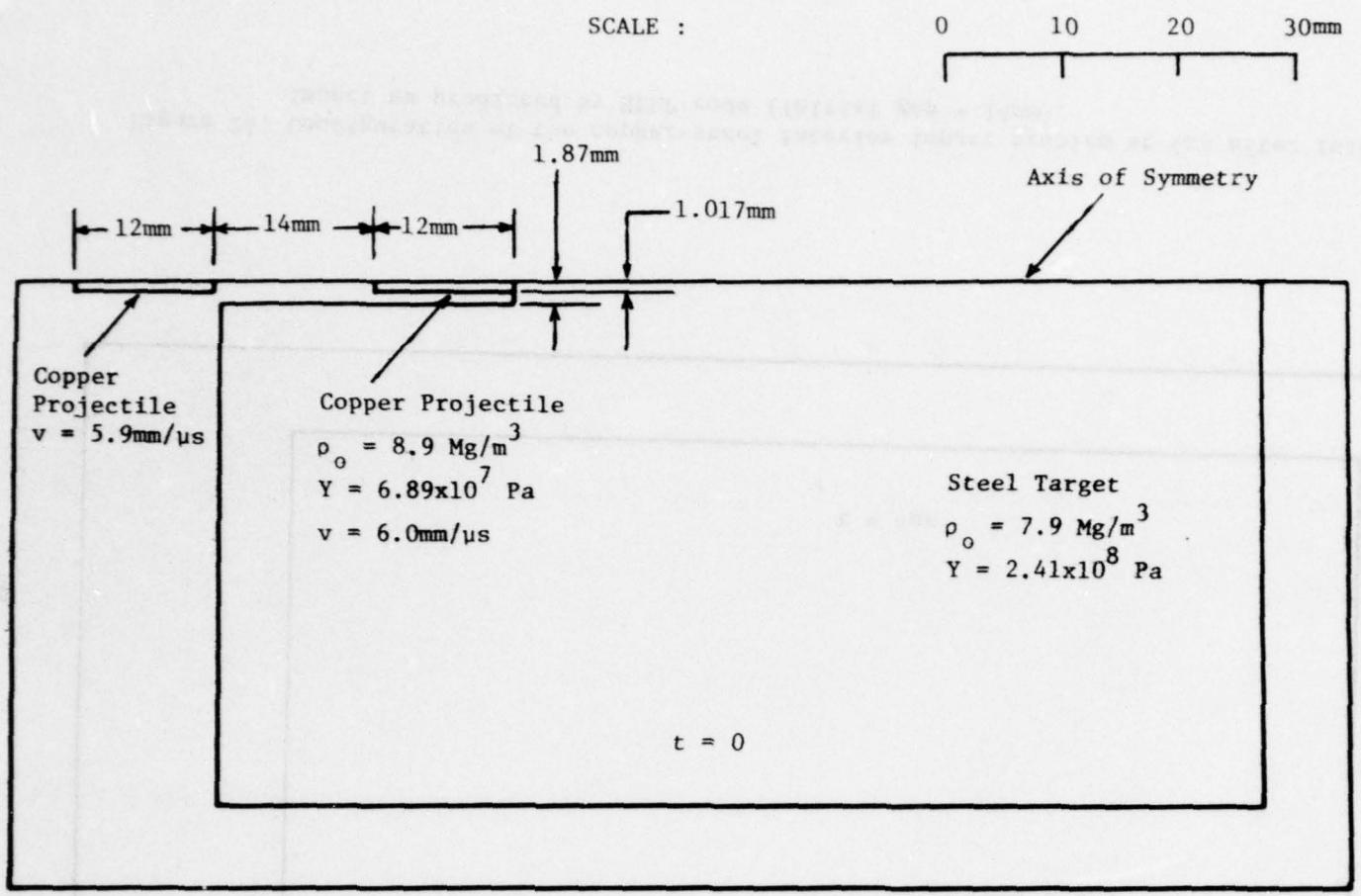

Figure 25. Initial configuration of the interior impact of copper projectiles onto a steel target (initial gap = 14mm).

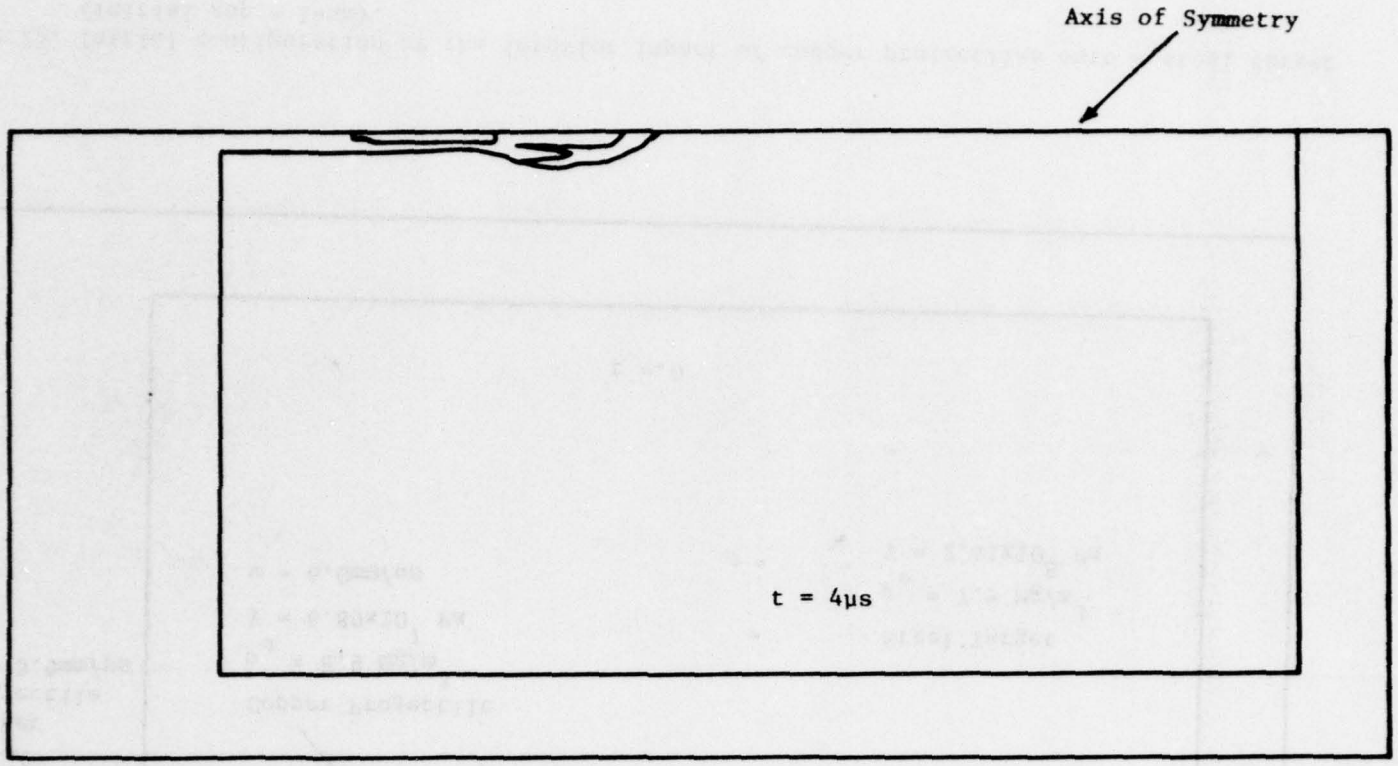

Figure 26. Configuration of the copper-steel interior impact problem at 4μs after initial impact as predicted by HELP code (initial gap = 14mm).

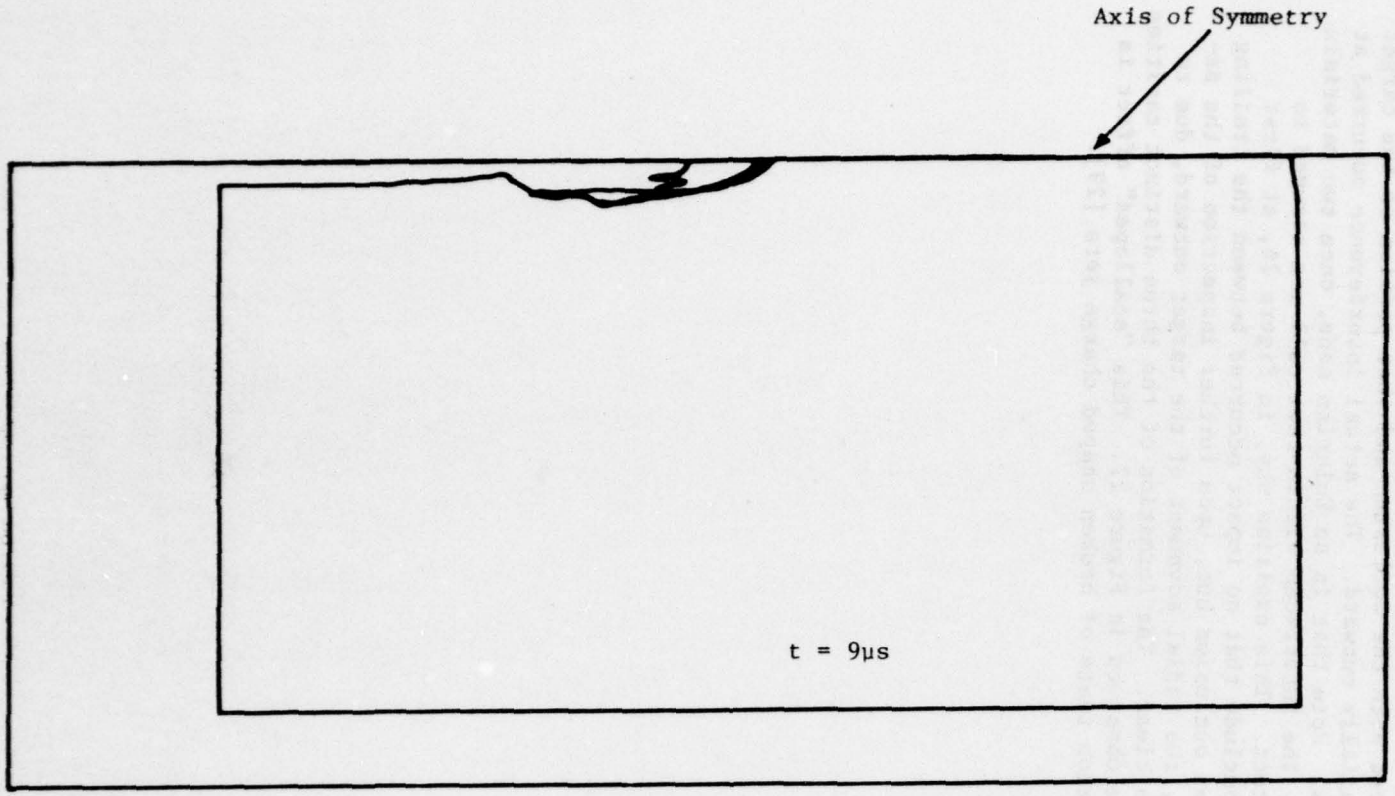

Figure 27. Configuration of the copper-steel interior impact at 9μs after initial impact (initial gap = 14mm).

In this set of computations we successfully showed that the trailing projectile does indeed interfere with the occlusion or "back flow" caused by the impact of the first. In Figure 26 the trailing projectile has already interfered with the occlusion and that portion of the target has begun to move radially outward. The actual interference occurred at a time prior to 4 μs. Note that in an Eulerian code, once two materials enter the same cell, the interfaces within that cell are assumed to impact or be in contact. This explains why, in Figure 26, at first glance, one might conclude that no impact occurred between the trailing projectile and target occlusion but, upon further inspection of the detailed calculations, the radial movement of the target outward, due to this impact, becomes clear. The formation of the three distinct cavities in the target can be observed in Figure 27. This "scalloped" effect is observed in penetration tests of broken shaped charge jets [29].

IV. CONCLUSIONS

We will now briefly present the major conclusions on the two tasks of this study, jet breakup and broken jet penetration. We will also give recommendations for continued work on these topics.

A. Stability and Breakup of Jets

In the study of jet breakup, we have formulated an analytical approach and have continued the numerical computations of our previous study [4]. A one-dimensional theory was formulated to solve the stretching jet problem subject to surface disturbances. The theory uses a strain hardening plastic model and assumes the surface disturbances to be small. Elastic loading and unloading is not included in the development. The theory yields a stability criterion which depends on the stress-strain curve. For an unstable jet, any small disturbance will grow. The theory also predicts the existence of a critical disturbance wavelength. That is, disturbances of this wavelength will grow faster than any other for a given set of conditions. For disturbances having this critical wavelength, the stability criterion states that at those times when the true stress is smaller than or equal to the slope of the true stress-true strain curve, the jet is stable; otherwise, it is unstable. For a perfectly plastic jet, the critical wavelength is always given by $(\lambda_0/2r_0)_{crit} = \pi\sqrt{2}$ regardless of material properties or strain rate. Furthermore, for perfectly plastic jets, if $\lambda_0/2r_0 > \pi/2$, the jet is always unstable. The theory also immediately reveals that disturbance growth rate in the jet increases as the strain rate η_0 decreases. Finally, the disturbance growth increases with the ratio of flow stress to density, σ_0/ρ_0.

Comparison with two-dimensional calculations indicates that the linearized one-dimensional theory predicts all the pertinent trends indicated by the two-dimensional results. The jet dimensions and strain rates used in the calculations are comparable to those observed in a typical jet from a BRL 81.3mm, 42°, copper-lined conical charge. The growth calculated from the theory appears reasonably accurate when the disturbance is initiated in the later stages of the shaped charge jet elongation process (i.e. when the strain rate is relatively low). For the earlier times after jet formation (i.e. when the strain rate is relatively high) the theoretical results are not adequate. Finally we note that the two-dimensional results indicate a dependence of critical wavelength to diameter ratio on the initial strain rate. We have found $\lambda_0/2r_0$ to vary between 1.5 for higher strain rates to 2.2 for lower strain rates in the jets studied here. However, the linearized theory predicts a value of $\lambda_0/2r_0 = 2.2$ regardless of strain rate. At present, we feel that these problems can be resolved by providing a more accurate solution to the theory. One method which appears very promising is to apply the linearized solution in a stepwise fashion for small increments of time taking care to match the proper conditions at each step.

The following are recommended areas for future work on jet atability and breakup:

1. The theory should be improved to account for growth at longer times after disturbance initiation, higher strain rates, and the affect of strain rate on critical wavelengths. as mentioned above, one approach would be to apply the present theory in a stepwise fashion for small increments of time and match the proper conditions between steps.

2. If the initial disturbance amplitude and its time of initiation are known, we can calculate the wavelength and amplitude at any later time. However, in a real jetting situation, we do not know precisely when to initiate the disturbance and at what amplitude. This must be known to predict the proper number of eventual jet particles.

3. We currently do not have a reliable method to determine how large the amplitude of a disturbance must grow to cause a break. "Brittle" jets and "ductile" jets may behave differently. This information is necessary to predict the eventual aspect ratio of the jet segments and the precise breakup time.

4. At present, we do not know precisely the instantaneous jet properties under impulsive and dynamic stretching conditions. Yielding, work hardening, rate effects, etc. will all play an important part in predicting disturbance growth and breakup in actual shaped charge jets.

B. Penetration Calculations

Various calculations of multiple interior impact were conducted to determine the mechanisms involved in the penetration of broken jets. The calculations involving lead projectiles and targets did not show the interference phenomenon expected. In fact, calculated penetrations were approximately 50% smaller than those observed in the experiments of [9]. At present, it is felt that this discrepancy is due to the anomalous behavior of the lead equation of state used in the code.

In the calculations of copper projectiles onto steel targets, the expected interference phenomenon was observed and the formation of three distinct cavities from two projectiles was shown. This may explain the "scalloped" hole formed when a target is penetrated by a broken shaped charge jet.

Though the expected penetration phenomenon was observed in the copper-steel case, the calculated hole size was smaller than expected. An attempt will be made to find out why this discrepancy exists and, if successful, any necessary modifications of the code will be made so that in future calculations it will be able to more accurately model these impact problems.

The next step is to compute the same copper-steel problem with no gap between the projectiles. This will demonstrate whether the penetration does indeed decrease significantly with increase in gap as shown in [7] and [8]. If it turns out that this gap effect is significant, then current penetration theories, which add up the segment length to compute penetration, should be modified to include a factor which also accounts for the gap.

Finally, it is recommended that future calculations include lower speed impacts (2-4 km/sec) of copper projectiles on steel targets aimed at determining the proper "cutoff" criterion of jet penetration. Also HELP code penetration calculations of continuous jets having a velocity gradient along their length should also be undertaken.

V. REFERENCES

1. Chou, P.C. and Carleone, J., "Calculation of Shaped Charge Jet Strain, Radius, and Breakup Time," U.S. Army Ballistic Research Laboratories (BRL) Contract Report No. 246, July 1975. (AD #B007240L)

2. Carleone, J. and Chou, P.C., "A One-Dimensional Theory to Predict the Strain and Radius of Shaped Charge Jets," Proceedings of the First International Symposium on Ballistics, Orlando, Florida, Nov. 13-15, 1974.

3. Chou, P.C. and Carleone, J., "Breakup of Shaped Charge Jets," Proceedings of the 2nd International Symposium on Ballistics, Daytona Beach, Florida, March 9-11, 1976.

4. Chou, P.C., Carleone, J., Tanzio, C.A., and Ciccarelli, R.D., "Shaped Charge Jet Breakup Studies Using Radiograph Measurement and Surface Instability Calculations," Dyna East Corporation Technical Rept. DE-TR-76-1, July 30, 1976; also U.S. Army Ballistic Research Laboratories (BRL) Contract Report No. 337, April 1977. (AD #A040444)

5. Wilkins, M.L., "Calculation of Elastic-Plastic Flow," University of California, Lawrence Livermore Laboratory, Rept. UCRL-7322, Rev. 1, Jan. 24, 1969.

6. Karpp, R.R. and Simon, J., "An Estimate of the Strength of a Copper Shaped Charge Jet and the Effect of Strength on the Breakup of a Stretching Jet," U.S. Army Ballistic Research Laboratory Report No. 1893, June 1976. (AD #B012141L)

7. Chou, P.C., et al, "Experimental Study of Interior Impact," Mechanics and Structures Advanced Study Group Report No. 72-11, Drexel University June 1973.

8. Chou, P.C., Minnich, M., and Gause, L., "Experimental Study of Multiple Interior Impacts," U.S. Army Ballistic Research Laboratory Contractor Report No. 199, January 1975. (AD #B001400L)

9. Toland, R.H., Chou, P.C., and Leidel, D., "Interior Sequential Impact and Cylindrical Waves by Exploding Wire," U.S. Army Ballistic Research Laboratory Contractor Report No. 264, Oct. 1975. (AD #B007783L)

10. Chou, P.C. and Toland, R., "Experimental Study of Multiple Impacts," Experimental Mechanics, Vol. 17, No. 6, June 1977, pp. 201-206.

11. Hageman, L.J., and Walsh, J.M., "HELP, A Multi-Material Eulerian Program for Compressible Fluid and Elastic-Plastic Flows in Two Space Dimension and Time," U.S. Army Ballistic Research Laboratory Contractor Report No. 39, May 1971. Vol I - AD #726459, Vol II - AD #726460.

12. Pugh, E.M., Eichleberger, R.J., and Rostoker, N., "Theory of Jet Formation by Charges with Lined Conical Cavities," J. Appl. Physics, Vol. 23, No. 5, May 1952, pp. 532-536.

13. Eichelberger, R.J., "Experimental Test of the Theory of Penetration by Metallic Jets," J. Applied Physics, Vol. 27, No. 1, January, 1956, pp. 63-68.

14. DiPersio, R., Simon, J., and Martin, T.H., U.S. Army Ballistic Research Laboratory (BRL) Report No. 1298 (1960). (AD #629557)

15. Chou, P.C. and Carleone, J., "The Stability of Shaped Charge Jets" to appear in the J. Applied Physics, Sept. 1977, also Proceedings of the 3rd International Symposium on Ballistics, Karlsruhe, Federal Repurblic of Germany, March 23-25, 1977.

16. Lord Rayleigh, The Theory of Sound, 2nd ed., Vol. 2, Dover Pub., New York, 1945, pp. 351-363.

17. Bohr, N., Trans. Roy. Soc., 204(A), 281 (1909).

18. Boys, C.V., Soap Bubbles and the Forces which Mould Them (The Society for Promoting Christian Knowledge, London, 1916, reprinted by Doubleday, New York, 1959).

19. Weber, C., "Zum Zerfall eines Flussigheitsstrahles" (Disentegration of a Liquid Jet), Zeitschrift fur Angewandte Mathematik und Mechanik, Vol. 11, No. 2, April 1931, pp. 136-153.

20. Levich, V.G., Physicochemical Hydrodynamics, Prentice-Hall, 1962.

21. Chandrasekhar, S., Hydrodynamic and Hydromagnetic Stability (Oxford: The Clarendon Press 1961).

22. Tomotika, S., Proc. Roy. Soc., A153, 302 (1936).

23. Mikami, T., Cox, R.G., and Mason, S.G., "Breakup of Extending Liquid Threads," Post-Graduate Research Laboratory Report, Pulp and Paper Research Institute of Canada, PGRL/72, October 1974.

24. Courant, R., and Friedrichs, K.O., Supersonic Flow and Shock Waves (Interscience, New York, 1948).

25. Malvern, L.E., Introduction to the Mechanics of a Continuous Medium (Prentice-Hall, 1969).

26. Bridgman, P.W., "The Stress Distribution at the Neck of a Tension Specimen," Trans. of the ASM, Vol. 32, 1943, pp. 553-574.

27. Lubahn, J.D., and Felgar, R.P., Plasticity and Creep of Metals (John Wiley and Sons, 1961).

28. Karpp, R.R., Los Alamos Scientific Laboratory, Los Alamos, N.M. (private communication).

29. Merendino, A.B., and Vitali, R., "The Penetration of Shaped Charge Jets into Steel and Aluminum Targets of Various Strengths," U.S. Army Ballistic Research Laboratory Memorandum Report No. 1932, August 1968. (AD #392672)

30. Harrison, J., U.S. Army Ballistics Research Laboratory (private communication).

Appendix

In this appendix we will present the stress distribution for typical stretching jets subjected to a surface disturbance. Two stretching jet segments having a slight difference in initial disturbance and a slight difference in the initial mesh were simulated using the HEMP code. The stresses calculated are presented in both tabular and graphical form.

A. Tabular Display of Stresses as Predicted by HEMP Code for a Typical Stretching Jet.

In this section we tabulate stress data as computed by HEMP for the problem depicted in Fig. A1. The initial data for this problem is as follows:

initial density $\rho_0 = 8.9\ gm/cm^3$ yield strength $Y_0 = 0.2$ GPa

initial pressure $P_0 = 0$ shear modulus $G = 45.6$ GPa

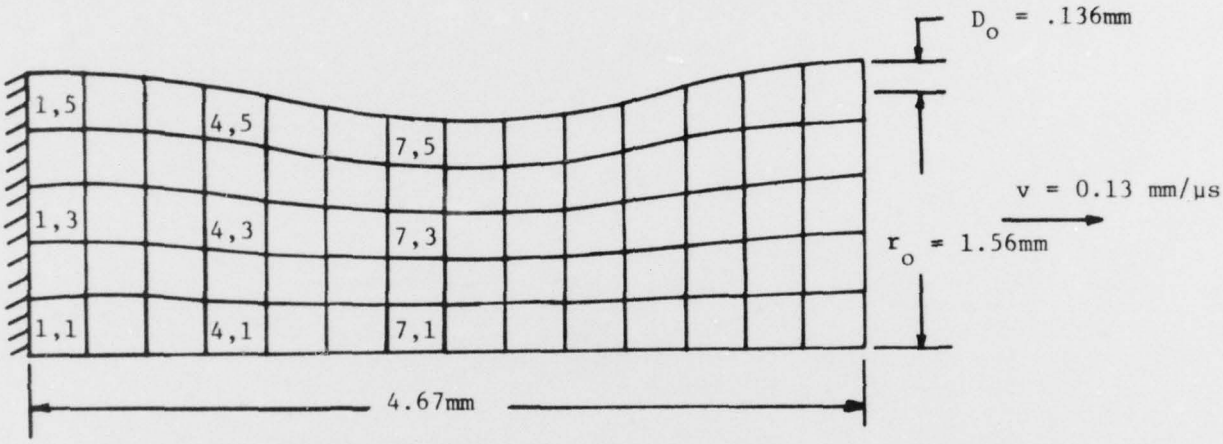

Figure A1. Initial geometry and grid layout for a typical HEMP calculation.

For this problem, the stresses as predicted by HEMP are listed as follows:

<u>t = .1 μs</u>

First time plane - all cells are plastic and have the same state of stress*

P	S_{xx}	S_{rr}	$S_{\theta\theta}$	σ_{xx}	σ_{rr}	$\sigma_{\theta\theta}$
-3.26	1.33	-6.67	-6.67	4.59	2.59	2.59

where

P denotes pressure

S denotes the stress deviator components

and σ denotes the stress components

$$\sigma_{ij} = -P + S_{ij}$$

* <u>NOTE</u>: All stresses and pressures tabulated are in 10^8 Pa(k bar)

t = .2 μsec

All cells are plastic

(J,K)	P	S_{xx}	S_{rr}	$S_{\theta\theta}$	σ_{xx}	σ_{rr}	$\sigma_{\theta\theta}$
(1,5)	-1.14	1.23	-1.05	-0.18	2.37	0.09	0.96
(1,3)	-6.28	1.33	-0.67	-0.67	7.61	5.61	5.61
(1,1)	-6.28	1.33	-0.67	-0.67	7.61	5.61	5.61
(4,5)	-0.83	1.20	-1.00	-0.19	2.03	-0.17	0.63
(4,3)	-6.28	1.33	-0.67	-0.67	7.61	5.61	5.61
(4,1)	-6.28	1.33	-0.67	-0.67	7.61	5.61	5.61
(7,5)	-0.79	1.25	-1.02	-0.23	2.04	-0.23	0.56
(7,3)	-6.28	1.33	-0.67	-0.67	7.61	5.61	5.61
(7,1)	-6.28	1.33	-0.67	-0.67	7.61	5.61	5.61

t = .3 μsec

All cells are plastic

(J,K)	P	S_{xx}	S_{rr}	$S_{\theta\theta}$	σ_{xx}	σ_{rr}	$\sigma_{\theta\theta}$
(1,5)	-1.90	1.32	-0.50	-0.82	3.22	1.40	1.08
(1,3)	-7.22	1.29	-0.93	-0.36	8.50	6.29	6.85
(1,1)	-10.0	1.33	-0.67	-0.67	11.33	9.33	9.33
(4,5)	-2.40	1.28	-0.51	-0.77	3.68	1.88	1.16
(4,3)	-6.50	1.27	-0.95	-0.32	7.77	5.55	6.18
(4,1)	-10.0	1.33	-0.67	-0.67	11.33	9.33	9.33
(7,5)	-2.42	1.33	-0.67	-0.64	3.75	1.73	1.78
(7,3)	-5.88	1.28	-0.97	-0.30	7.16	4.90	5.58
(7,1)	-10.0	1.33	-0.67	-0.67	11.33	9.33	9.33

t = .4 μsec

All cells are plastic

(J,K)	P	S_{xx}	S_{rr}	$S_{\theta\theta}$	σ_{xx}	σ_{rr}	$\sigma_{\theta\theta}$
(1,5)	-0.97	1.32	-0.54	-0.78	2.29	0.43	0.19
(1,3)	-4.37	1.31	-0.87	-0.43	5.67	3.20	4.07
(1,1)	-10.0	1.33	-0.67	-0.67	11.33	9.33	9.33
(4,5)	-0.66	1.27	-0.68	-0.59	1.93	-0.02	0.07
(4,3)	-4.20	1.32	-0.74	-0.58	5.52	3.46	3.62
(4,1)	-10.0	1.33	-0.67	-0.67	11.33	9.33	9.33
(7,5)	-0.62	1.33	-0.76	-0.56	1.95	-0.14	0.06
(7,3)	-4.34	1.33	-0.59	-0.74	5.67	3.75	3.60
(7,1)	-10.0	1.33	-0.67	-0.66	11.33	9.33	9.34

t = 11.1 μsec

All cells are plastic

(J,K)	P	S_{xx}	S_{rr}	$S_{\theta\theta}$	σ_{xx}	σ_{rr}	$\sigma_{\theta\theta}$
(1,5)	0.21	1.28	-0.32	-0.96	1.06	-0.54	-1.17
(1,3)	2.19	1.33	-0.58	-0.75	-0.86	-2.77	-2.94
(1,1)	3.36	1.33	-0.67	-0.66	-2.03	-4.03	-4.02
(4,5)	-0.23	1.24	-0.52	-0.72	1.47	-0.29	-0.49
(4,3)	1.21	1.31	-0.60	-0.71	0.10	-1.80	-1.92
(4,1)	2.03	1.33	-0.67	-0.67	-0.70	-2.70	-2.70
(7,5)	-0.58	1.33	-0.66	-0.67	1.91	-0.08	-0.09
(7,3)	-1.47	1.33	-0.66	-0.67	2.80	0.81	0.80
(7,1)	0.15	1.33	-0.67	-0.67	1.18	-0.82	-0.82

t = 11.2 μsec

All cells are plastic
except where noted

(J,K)	P	S_{xx}	S_{rr}	$S_{\theta\theta}$	σ_{xx}	σ_{rr}	$\sigma_{\theta\theta}$
(1,5)	0.07	1.30	-0.40	-0.90	1.23	-0.46	-1.03
*(1,3)	1.96	1.31	-0.60	-0.71	-0.65	-2.56	-2.67
*(1,1)	2.99	1.25	-0.63	-0.62	-1.74	-3.62	-3.61
(4,5)	-0.36	1.22	-0.62	-0.60	1.58	-0.26	-0.24
(4,3)	0.96	1.28	-0.63	-0.65	0.32	-1.59	-1.60
(4,1)	1.75	1.33	-0.67	-0.66	-0.42	-2.42	-2.41
(7,5)	-0.66	1.33	-0.68	-0.65	1.99	-0.02	0.01
(7,3)	-0.43	1.33	-0.67	-0.65	1.76	-0.24	-0.22
(7,1)	-0.27	1.33	-0.67	-0.67	1.60	-0.94	-0.93

*These cells are elastic

t = 11.3 μsec

All cells are plastic
except where noted

(J,K)	P	S_{xx}	S_{rr}	$S_{\theta\theta}$	σ_{xx}	σ_{rr}	$\sigma_{\theta\theta}$
(1,5)	-0.37	1.33	-0.64	-0.69	1.70	-0.27	-0.32
*(1,3)	0.80	1.16	-0.59	-0.57	0.36	-1.40	-1.37
*(1,1)	1.46	1.04	-0.53	-0.51	-0.42	-1.99	-1.97
(4,5)	-0.68	1.19	-0.73	-0.46	1.87	-0.05	0.22
(4,3)	0.05	1.24	-0.67	-0.57	1.19	-0.72	-0.62
(4,1)	0.43	1.33	-0.67	-0.66	0.90	-1.09	-1.09
(7,5)	-0.76	1.32	-0.69	-0.63	2.08	0.07	0.13
(7,3)	-0.93	1.33	-0.68	-0.65	2.33	0.32	0.35
(7,1)	-1.02	1.33	-0.67	-0.67	2.35	0.35	0.35

*These cells are elastic

B. Graphical Presentation of Axial Stresses in a Typical Stretching Jet

In this section we will graphically display the stress data as calculated using the HEMP code for the problem depicted in Figure A2. All other initial data the same as the previous problem in part A of appendix.

The following pages contain plots of axial stress (σ_x) vs. time for the cells specified.

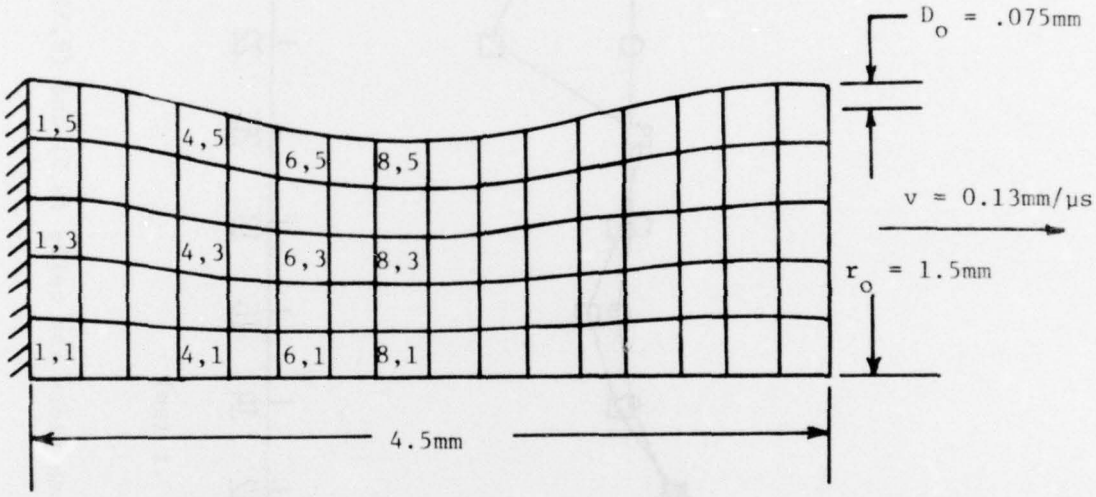

Figure A2. Initial geometry and grid layout for a typical HEMP calculation.

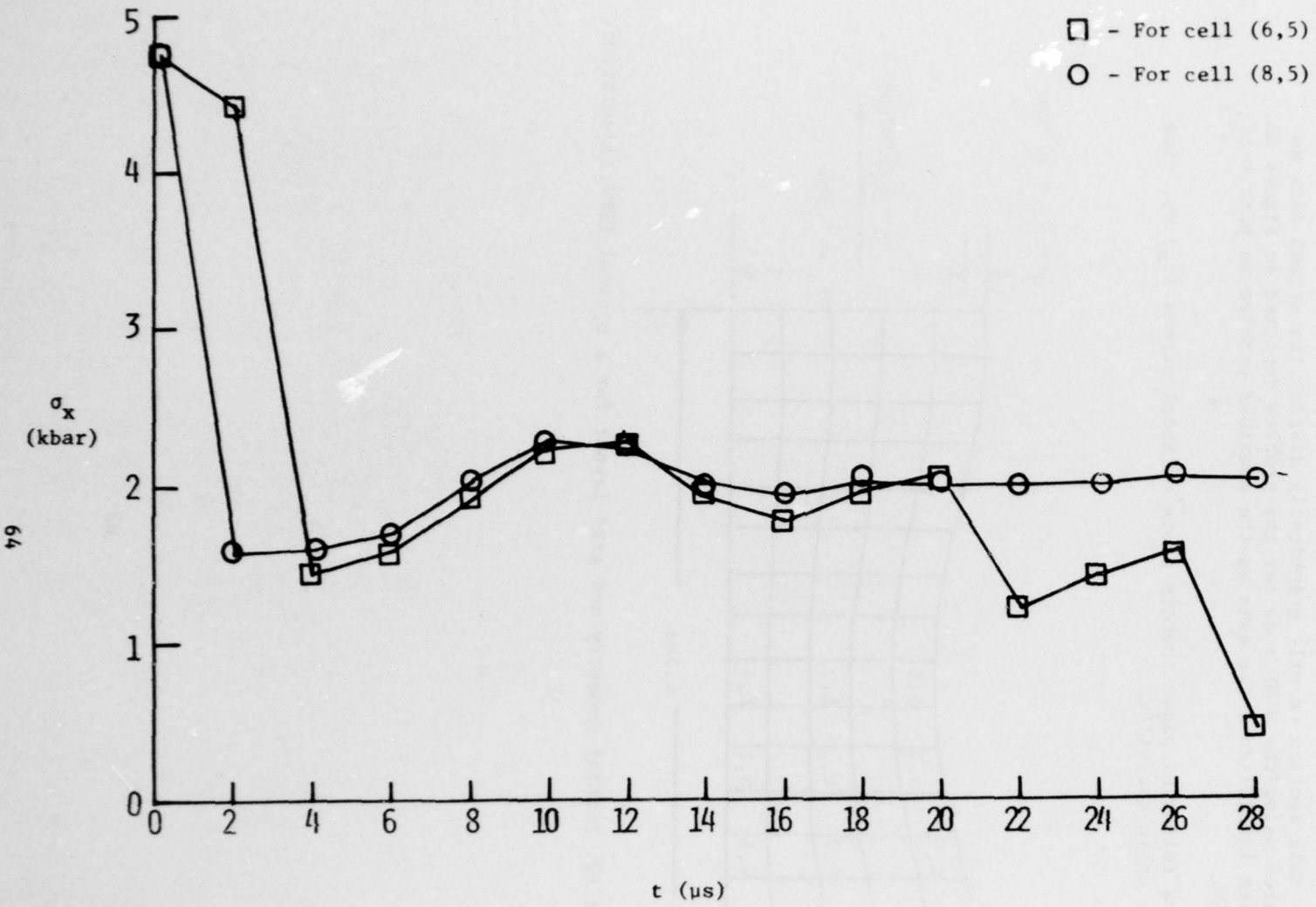

Figure A3. Axial stress vs. time plots for cells (6,5) and (8,5) as defined in Figure A2.

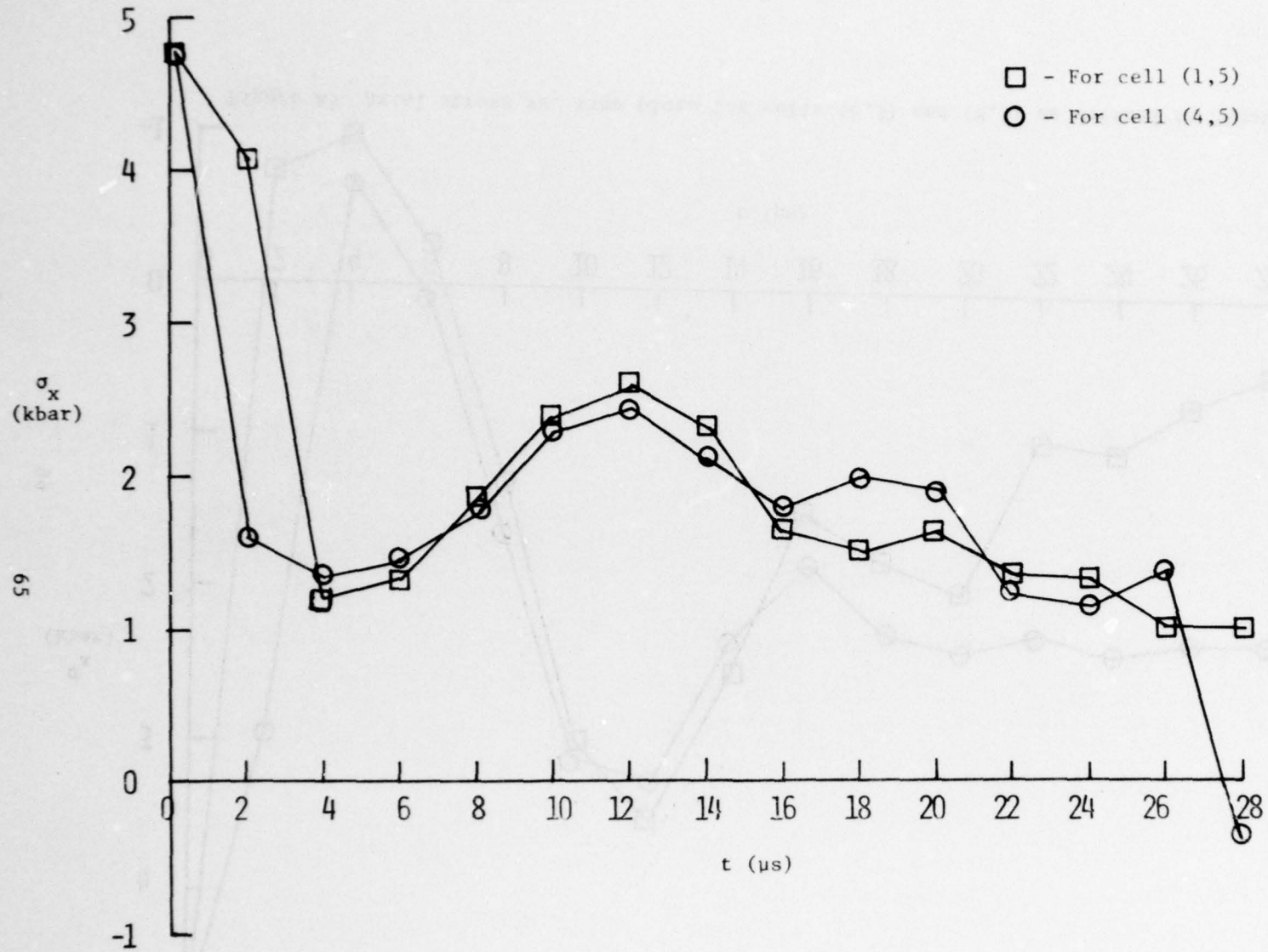

Figure A4. Axial stress vs. time plots for cells (1,5) and (4,5) as defined in Figure A2.

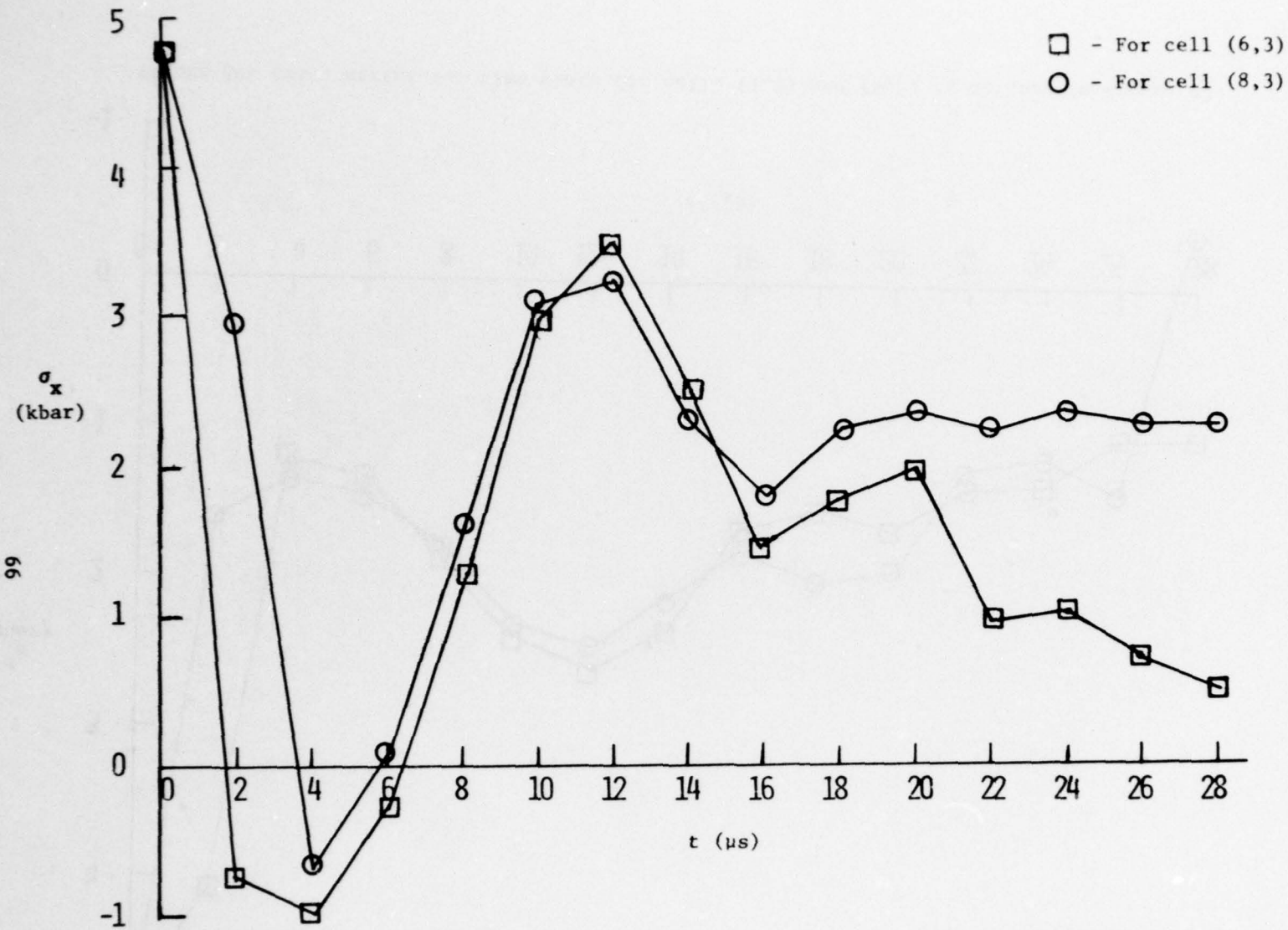

Figure A5. Axial stress vs. time plots for cells (6,3) and (8,3) as defined in Figure A2.

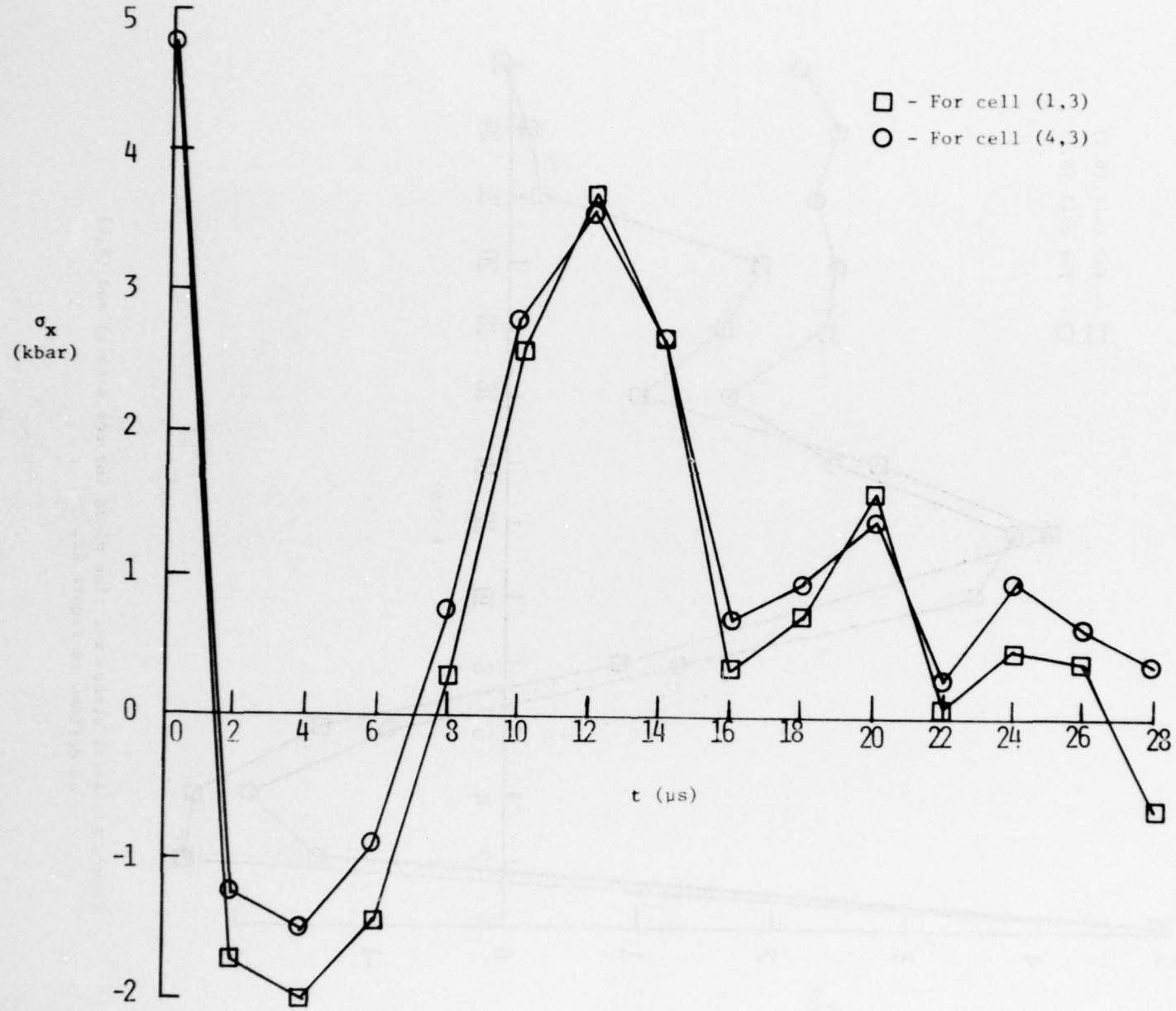

Figure A6. Axial stress vs. time plots for cells (1,3) and (4,3) as defined in Figure A2.

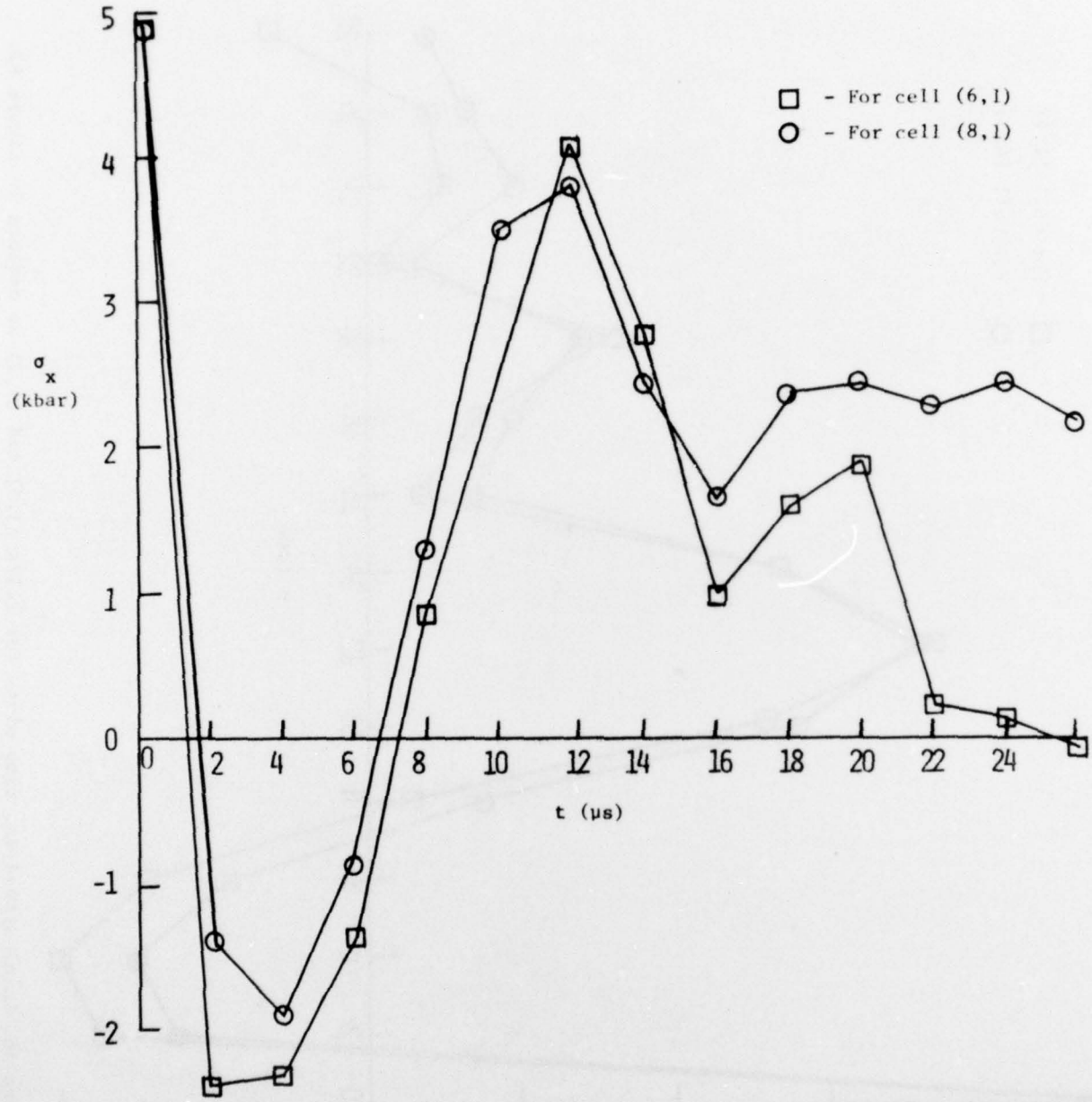

Figure A7. Axial stress vs. time plots for cells (6,1) and (8,1) as defined in Figure A2.

DISTRIBUTION LIST

No. of Copies	Organization
12	Commander Defense Documentation Center ATTN: DDC-TCA Cameron Station Alexandria, VA 22314
1	Commander US Army Materiel Development and Readiness Command ATTN: DRCDMA-ST 5001 Eisenhower Avenue Alexandria, VA 22333
1	Commander US Army Aviation Research and Development Command ATTN: DRSAV-E 12th and Spruce Streets St. Louis, MO 63166
1	Director US Army Air Mobility Research and Development Laboratory Ames Research Center Moffett Field, CA 94035
1	Commander US Army Electronics Command ATTN: DRSEL-RD Fort Monmouth, NJ 07703
1	Commander US Army Missile Research and Development Command ATTN: DRDMI-R Redstone Arsenal, AL 35809
1	Commander US Army Tank Automotive Development Command ATTN: DRDTA-RWL Warren, MI 48090
2	Commander US Army Mobility Equipment Research & Development Command ATTN: Tech Docu Cen, Bldg. 315 DRSME-RZT Fort Belvoir, VA 22060
1	Commander US Army Armament Materiel Readiness Command Rock Island, IL 61202
6	Commander US Army Armament Research and Development Command ATTN: DRDAR Mr. T. Stevens Mr. G.Randers-Pehrson Dr. N. Clark Mr. J. Hershkowitz Mr. J. Pearson Tech Lib Dover, NJ 07801
1	Commander US Army Harry Diamond Labs ATTN: DRXDO-TI 2800 Powder Mill Road Adelphi, MD 20783
2	Commander US Army Materials and Mechanics Research Center ATTN: DRXMR-RF, J. Mescall Tech Lib Watertown, MA 02172
1	Director US Army TRADOC Systems Analysis Activity ATTN: ATAA-SL (Tech Lib) White Sands Missile Range NM 88002

DISTRIBUTION LIST

No. of Copies	Organization
1	Assistant Secretary of the Army (R&D) ATTN: Asst for Research Washington, DC 20310
2	HQDA (DAMA-ZA; DAMA-AR) Washington, DC 20310
1	Commander US Army Research Office P. O. Box 12211 Research Triangle Park NC 27709
2	Commander US Naval Air Systems Command ATTN: Code AIR-310 Code AIR-350 Washington, DC 20360
1	Commander US Naval Ordnance Sys Command ATTN: Code ORD-0332 Washington, DC 20360
2	Chief of Naval Research Department of the Navy ATTN: Code 427 Code 470 Washington, DC 20325
1	Commander US Naval Surface Weapons Center ATTN: Code 730, Lib Silver Spring, MD 20910
2	Commander US Naval Surface Weapons Center ATTN: Code DG-50 Tech Lib Dahlgren, VA 22448
1	Commander US Naval Weapons Center ATTN: Code 45, Tech Lib China Lake, CA 93555
1	Commander US Naval Research Laboratory Washington, DC 20375
1	USAF/AFRDDA Washington, DC 20311
1	AFSC/SDW Andrews AFB Washington, DC 20311
1	US Air Force Academy ATTN: Code FJS-41 (NC) Tech Lib Colorado Springs, CO 80840
1	AFWL (SUL, LT Tennant) Kirtland AFB, NM 87116
1	AFLC/MMWMC Wright-Patterson AFB, OH 45433
1	AFAL/AVW Wright-Patterson AFB, OH 45433
6	Director Lawrence Livermore Laboratory ATTN: Dr. J. Kury Dr. M. Wilkins Dr. E. Lee Dr. H. Hornig Dr. J. Knowles Tech Lib P. O. Box 808 Los Alamos, NM 87544

DISTRIBUTION LIST

No. of Copies	Organization
1	Battelle Columbus Laboratories ATTN: Mr. Joseph E. Backofen 505 King Avenue Columbus, OH 43201
4	Dyna East Corporation ATTN: P. C. Chou J. Carleone C. A. Tanzio R. D. Cicarelli 227 Hemlock Road Wynnewood, PA 19096
1	Honeywell, Inc. Government and Aeronautical Products Division ATTN: C. R. Hargreaves 600 Second Street Hopkins, MN 55343
1	Physics International Corp ATTN: Dr. L. Berhman 2700 Merced Street San Leandro, CA 94577
1	Sandia Laboratories ATTN: Dr. W. Herrmann Albuquerque, NM 87115
1	Shock Hydrodynamics ATTN: Dr. L. Zernow 4710-4716 Vineland Avenue North Hollywood, CA 91602

No. of Copies	Organization
1	Systems, Science & Software ATTN: Dr. R. Sedgwick P. O. Box 1620 La Jolla, CA 92037
1	Drexel Institute of Technology Wave Propagation Research Center ATTN: Prof. P. Chou Philadelphia, PA 19104
2	University of California Los Alamos Scientific Lab ATTN: Dr. J. Walsh Tech Lib P. O. Box 1663 Los Alamos, NM 87544
1	University of Dayton Research Institute ATTN: Dr. Stephen J. Bless Dayton, OH 45469

Aberdeen Proving Ground

Marine Corps Ln Ofc
Dir, USAMSAA